



~~91-09527~~

AD-A149 381

SEMI-ANNUAL TECHNICAL REPORT

31 January 1979 - 30 June 1979

LASER ASSISTED SEMICONDUCTOR DEVICE PROCESSING

This research was sponsored by the
Defense Advanced Research Projects
Agency under ARPA Order No. 3578
Contract No. MDA903-78-C-0284
Monitored by: Dr. Isaac Lagnado
Naval Ocean Systems Center
Contract Duration: 1 June 1978 - 30 November 1979

6 November 1979

APPROVED FOR PUBLIC RELEASE;
DISTRIBUTION IS UNLIMITED (A)

DTIC
ELECTE
JAN 09 1985
S D E

TRW

Defense and Space Systems Group

One Space Park • Redondo Beach • California • 90278

84 12 28 005

DTIC FILE COPY

SEMI-ANNUAL TECHNICAL REPORT

31 January 1979 - 30 June 1979

LASER ASSISTED SEMICONDUCTOR DEVICE PROCESSING

This research was sponsored by the
Defense Advanced Research Projects
Agency under ARPA Order No. 3578
Contract No. MDA903-78-C-0284
Monitored by: Dr. Isaac Lagnado
Naval Ocean Systems Center
Contract Duration: 1 June 1978 -
30 November 1979

The views and conclusions contained in this document are those of the author(s) and should not be interpreted as necessarily representing the official policies, either express or implied, of the Defense Advanced Research Projects Agency or the United States Government.

TRW Defense and Space Systems Group
One Space Park
Redondo Beach, CA 90278

DTIC
ELECTE
JAN 09 1985
S D
E

CONTENTS

	<u>Page</u>
SUMMARY	1
TASK 1 - LASER INDUCED SURFACE PROCESSING	3
1. INTRODUCTION	3
2. RESULTS	4
2.1 The Effect of Damage on Laser Heating	4
2.2 Laser Annealing of Low Fluence Ion-Implanted Silicon	5
TASK 2 - LASER BLOW-OFF ION IMPLANTATION	8
3. INTRODUCTION	8
4. TECHNICAL DISCUSSION	10
4.1 Technique	10
4.2 Experimental Apparatus	12
4.3 Results	17
REFERENCES	30
APPENDIX A - THE EFFECT OF CARRIER DIFFUSION ON LASER-HEATING OF LIGHTLY DAMAGED SEMICONDUCTORS; and	A1
APPENDIX B - LASER ANNEALING OF LOW FLUENCE ION IMPLANTED SILICON	B1

Accession For	
NTIS GRA&I	<input checked="checked" type="checkbox"/>
DTIC TAB	<input type="checkbox"/>
Unannounced	<input type="checkbox"/>
Justification	
By _____	
Distribution/	
Availability Codes	
Dist	Avail and/or Special
A-1	



ILLUSTRATIONS

<u>Figure</u>		<u>Page</u>
1a	Schematic Diagram of Laser Blow-Off Ion Implantation System	13
1b	Photograph of Laser Blow-Off Ion Implantation System	14
2	Geometric Arrangement for the Theoretical Model and Experiment	20
3	Theoretical Curves for Beam Particle Current Density \vec{J} versus Time, Normalized to the Time at which \vec{J} is a Maximum	22
4	Unaccelerated Boron Ion Pulses	23
5	Theoretical Curves for $\int_0^{\theta} \vec{J} dt$ versus Detector Angle θ at Constant Distance r and Normalized to the Value for $\theta = 0$	24
6	Applied Research Laboratories IMMA (Ion Microprobe Mass Analyzer)	27
7	Boron/Silicon Depth Profile	29

SUMMARY

The objective of Task 1 of this program is to evaluate and characterize laser-induced processing of semiconductor materials and devices. The work described here was performed under Contract No. MDA 903-78-C-0284 during the period of February 1979 to July 1979. The previous work performed during the period of June 1978 to January 1979 was already described in the semi-annual technical report "Laser Assisted Semiconductor Device Processing," No. 33292.000.

The TRW contribution to laser-induced processing of semiconductor surfaces consisted of the demonstration of the effect of lattice damage on the laser-induced heating,¹ and the development of annealing techniques for lightly damaged materials.² This new technique, pioneered at TRW, consists of combining a laser anneal with a short low temperature thermal anneal. It exploits the unique ability of laser processing to dissolve lattice defects without providing sufficient energy for melting or regrowth. A detailed discussion of the effect of damage on the laser-induced heating is given in Section 2.1 and Appendix A.

In our new technique, the sample is first irradiated by a pulsed laser. This removes lattice defects. This defect-free material is then subjected to a moderate thermal anneal. This results in full electrical activation without significant change in the impurity distribution. Thus, by combining laser irradiation with short low temperature thermal anneal, it is possible to both eliminate defects and electrically activate lightly damaged semiconductors. Since melting is avoided, the dopant distribution remains as implanted. The results of these experiments are summarized in Section 2.2 and Appendix B. Preliminary experiments have also shown that this technique can be applied to high fluence implants.

The objective of Task 2 is to evaluate the laser blow-off ion implantation source.

This new ion implantation technique utilizes pulsed laser irradiation of a solid surface of pure dopant material to produce a high temperature plasma of dopant ions. The plasma expands into vacuum, reducing the charge density to the point where an externally applied electric field can be used to extract ions from the plasma. In principle, these ions can be accelerated to an arbitrarily high energy and can be used to implant semiconductor materials. A subtle aspect of this method is the pulsed nature of the ion beam current. For reasonable values of ion energy and ion areal density, it appears that annealing temperatures can be reached in the implanted regions for very short times at each laser pulse.

Measurements have been made and results obtained largely in the order of laser performance, implant plasma production, plasma plume characteristics, ion current and areal uniformity, implant material deposition without acceleration, and implant with high energy implant ions.

TASK 1. LASER INDUCED SURFACE PROCESSING

1. INTRODUCTION

In our work at TRW, we have investigated the important difference between annealing of heavily and lightly damaged materials. Our original results confirmed findings recently reported in the literature: for lightly damaged samples, the crystal regrowth was poor, and only partial electrical activation was obtained, though the displacement damage was removed. In contrast, for high fluence samples, excellent activation was obtained.

The mechanism for the Q-switched laser annealing is believed to involve melting of the amorphized surface followed by liquid phase regrowth.^{3,4} Here, the defects are almost completely removed and a full activation of dopants at concentrations far exceeding the equilibrium limit of solid solubility has been reported.⁵ This method has its biggest potential in applications where slight changes in the implanted profiles can be tolerated. This is because melting results in some impurity redistribution. For ruby annealed silicon samples, typical profile widths are around 0.3 μm .^{1,5}

Our early experiments lead us to thoroughly investigate the effect of damage on the laser-induced heating. For the theoretical effort, we have developed a model¹ which explains the observed differences between annealing of heavily and lightly damaged surfaces. This is done by taking into account diffusion of the photoexcited carriers. This is discussed in Section 2.1 and Appendix A. In our experimental effort, we have subsequently developed a novel technique² which permits laser annealing of lightly damaged materials. This has the very attractive feature of maintaining the as-implanted impurity profiles. This is discussed in Section 2.2 and Appendix B. Preliminary experiments have also shown that this technique can be applied to high fluence implants.

2. RESULTS

2.1 THE EFFECT OF DAMAGE ON LASER HEATING

The conversion of optical to thermal energy during laser-annealing consists of two major processes:

- Absorption of laser light
- Conversion of absorbed optical energy to heat.

In strongly absorbing semiconductors, the dominant absorption mechanism at frequencies higher than the bandgap frequency is interband transitions. The absorbed energy is released to heat through the thermalization of the photoexcited carriers, i.e., heat is distributed into a depth comparable to carrier diffusion length. In good quality materials, the carrier diffusion lengths are longer than the optical absorption depth. Thus, the heating volume is enlarged, and for the same laser power, the average temperature is lower than in heavily damaged material.

The carriers recombine preferentially at defect sites, producing localized thermal spikes. If the density of the non-radiative recombination centers is high, the average temperature is high. This is the case in heavily damaged materials. At these elevated temperatures epitaxial regrowth (liquid phase) and impurity activation occur. If the density is low, the average temperature is low. This is the case in lightly damaged materials. Here the application of laser fluxes equivalent to that used in high fluence implants produces no melting in low fluence implants. No regrowth and little or no dopant activation occur even though the defects dissolve due to the preferential supply of energy at the defect sites. Thus, it is possible in lightly damaged materials to remove the displacement damage even without providing sufficient average energy to activate implanted impurities.

Our detailed thermal analysis supports this picture. We have developed a model¹ which explains the observed differences between annealing of lightly and heavily damaged materials by

taking into account the diffusion of the photoexcited carriers. Previous thermal models were concerned with heavily damaged materials, in that they assumed that the absorbed optical energy is converted to heat in the immediate vicinity of the absorbed photons. In our work, the time evolution of temperature profiles was calculated for pulsed ruby and Nd:YAG illumination of silicon, and ruby illumination of GaAs. The material, optical, and electronic properties were varied, to represent varied material quality. Surface recombination of the carriers was also taken into account. The effect of the damage on the heating was found to be much more pronounced for Nd:YAG than for ruby irradiation because a larger portion of the ruby laser energy (excess above bandgap) is given rapidly to the lattice through quasi-thermalization inside the semiconductor energy bands. Thermal spikes were formed as the result of the preferential recombination of the carriers at the surface. For a sufficiently fast surface recombination, the temperature profile may develop a secondary maximum in the bulk.

2.2 LASER ANNEALING OF LOW FLUENCE ION-IMPLANTED SILICON

The most successful applications of Q-switched lasers have been for annealing of high fluence implants.³ The method involves a pulsed laser such as a Q-switched Nd:YAG or ruby laser, with a typical pulse length between 10 and 200 nsec, and energy density between .5 and 3 J/cm². The annealing mechanism is believed to be melting of the amorphized surface followed by liquid phase regrowth.^{4,5} Here there is almost complete removal of defects and a full activation of dopant concentrations far exceeding the limit of solid solubility.^{3,5} However, this method can be only applied where slight changes in implanted profile can be tolerated. This is because melting results in some impurity redistribution. Typical profile widths in ruby laser annealed silicon are around 0.3 μm .^{3,6}

The second laser anneal method employs a cw laser operated in a scanning mode. For example, a 7W cw argon laser beam scanned at 2.76 cm/sec and producing lines of 22 μm width was

used to anneal to a 1000 Å depth in as-implanted silicon.⁷ The recrystallization is through solid state regrowth, because of the low powers and comparatively long anneal times. The dopant profiles are not changed by cw laser annealing.

The as-implanted impurity profiles can be maintained even in pulsed laser annealing by using techniques⁷ developed at TRW. These techniques consist of combined laser irradiation and low temperature thermal anneal. In our work at TRW we have systematically investigated the differences between annealing of lightly damaged materials and heavily damaged materials. We have applied ruby laser pulses of 1.5 to 2.5 J cm⁻² to silicon surfaces oriented in [100] and [111] directions and implanted with 10¹⁴ to 10¹⁵ B cm⁻² and 10¹⁴ to 5 x 10¹⁴ B cm⁻². Boron implantations were at 50 keV, phosphorus at 80 keV. It was found that laser energy densities used for high fluence implants did not produce melting or regrowth in the low fluence implants. Although the electrical activation was poor the lattice defects (e.g., dislocation loops) were removed. We have concluded that the average temperature induced in the lightly damaged material was substantially lower than the temperature induced in the heavily damaged material. This permitted only a small fraction of the implanted ions to migrate to substitutional positions. The damage was removed through the preferential heating at the defect sites.¹ However, when a sequential moderate thermal anneal, 10 min at 1000°C, was applied to these samples, a full electrical activation, and without significant impurity redistribution, was obtained. Thus, by combining a laser anneal with a short thermal anneal, it was possible to achieve defect elimination as well as complete electrical activation. This was the first reported² successful use of pulsed laser radiation for annealing of low fluence implants.

Preliminary experiments have shown that we can also apply these techniques to high fluence implants. One type of implantation, that of 5 x 10¹⁴ P cm⁻² into a [111] surface, resulted in amorphism. Our early experiments as well as others in the literature showed that irradiation of amorphized surfaces

by a Q-switched ruby laser results in melting. Thus, in order to avoid melting, the damaged region should first be recrystallized. This was done by introducing a moderate thermal anneal before the irradiation. To date, the best results were obtained with a two-step thermal anneal, 30 min at 550°C, and 10 min at 1000°C. This caused the amorphous layer to regrow into single crystallinity by solid phase epitaxy. The subsequent irradiation eliminated defects without melting. Not only did we eliminate the defects, but by avoiding melting, we also maintained the desirable as-implanted impurity profiles.

The demonstrated techniques have an enormous potential for practical applications. Low fluence implants account for more than 50 percent of the potential implant uses since all bases for junction transistors fall into this category. The ability to anneal high fluence implants without dopant redistribution is important for the production of shallow emitters, which are essential for an entire category of devices, such as microwave transistors. The ability to anneal material without changing the implanted profiles would permit full exploitation of the ion-implant unique capability of creating narrow accurately controlled impurity profiles.

TASK 2. LASER BLOW-OFF ION IMPLANTATION

3. INTRODUCTION

A new, potentially less expensive, and relatively simple technique for ion implantation of extended areas of semiconductor material has been conceived and is being experimentally developed under contract to DARPA. This new method involves a source of implant ions produced by laser "blow-off" from a piece of dopant material. Energy from a short-pulse laser is focused onto the surface of the dopant material, forming a small bubble of dopant plasma which "blows off." This plasma bubble is allowed to expand into vacuum until its density and area become suitable for electrostatic acceleration to the necessary ion implant energy. Key features include the easy formation of intense ion beams of virtually any dopant material, with beam areas of several inch diameter, and without the necessity for slower and more expensive rastering of ion beams from sophisticated ion beam machines. Perhaps most significant, although also more speculative, is the potential for self-annealing of implant damage during the implant process. This possibility arises from the unique situation of the short pulse of the high intensity, high energy ion beam, which rapidly deposits energy exactly in the implant region to momentarily raise the material temperature. If this possibility can be realized in practice, an entire and sometimes troublesome separate annealing process normally associated with ion implantation can be eliminated.

Thus far an apparatus has been built and tested for implanting ions by this method. Implants of boron ions into silicon substrates have been made at energies up to 50 keV. The upper energy was limited by electrical breakdown across inadequate vacuum feed-throughs, a problem which is being corrected. The quality of the implants is being assayed with Ion Microprobe Mass Analysis (IMMA) equipment. The IMMA measurements are ideal for determining

precisely the implant ion depth profiles and surface areal uniformity, and provide meaningful comparisons between the new and the conventional methods. In fact, IMMA has been more appropriate as a diagnostic than actual semiconductor device fabrication tests to this time, since the success or failure of device fabrication may say little about large and small scale uniformity and overall depth profiles which have been our initial concern. Major emphasis has therefore been placed on the IMMA evaluation technique up to now.

In the next contract period, major emphasis will be shifted from IMMA as diagnostic to the quality of actual semiconductor devices fabricated with the laser blow-off implantation technique and to C-V type measurements. This shift is particularly important in studying the self-annealing feature of the new method since IMMA can say little about semiconductor structure and activation properties. And in the final analysis the quality of the fabricated semiconductor device operation is clearly the key measure of success.

4. TECHNICAL DISCUSSION

4.1 TECHNIQUE

Ion implantation of dopants in semiconductor materials has become a standard practice in the manufacture of solid state electronic devices. Ion implantation is a non-equilibrium process that permits a degree of control over the spatial distribution of dopant atoms in the host crystal that cannot be achieved through thermal diffusion. Dopant species with low diffusion rates even at elevated temperatures can often be handled with relative ease through ion implantation. However, a deleterious side effect of ion implantation is damage to the host crystal caused by the high energy ions necessary to penetrate to the desired depths. High temperature annealing is commonly used to repair implant-induced damage. In some cases the annealing process itself causes a degradation of the implanted material. For example, high temperature annealing of implanted GaAs results in migration of As atoms from the crystal. In large scale integrated circuits, heat treating may alter the properties of the intrinsic material at locations remote from ion implanted sites. The following part of this report describes progress towards developing a new ion implantation technique which shows promise of providing a self-annealing feature as well as being relatively simple, fast, with large areal coverage and amenable to a very wide range of dopant species.

This new ion implantation technique utilizes pulsed laser irradiation of a solid surface of pure dopant material to produce a high temperature plasma of dopant ions. The plasma expands into vacuum, reducing the charge density to the point where an externally applied electric field can be used to extract ions from the plasma. In principle these ions can be accelerated to an arbitrarily high energy and can be used to implant semiconductor

materials. A subtle aspect of this method is the pulsed nature of the ion beam current. For reasonable values of ion energy and ion areal density, it appears that annealing temperatures can be reached in the implanted regions for very short times at each laser pulse. Thus the possibility presents itself that the use of high intensity short duration ion beam pulses for ion implantation may be accompanied by self-annealing of the implant damage. One of the main objectives of this program is to carefully examine this possibility experimentally by systematically evaluating the characteristics of semiconductor devices implanted with this laser blow-off technique over a variety of practical conditions.

4.2 EXPERIMENTAL APPARATUS

A schematic diagram and picture of the ion implantation system developed here is shown as Figures 1a and 1b. This system is an adaptation of the high intensity metal ion beam source described in Reference 8. The ions to be implanted are created by pulsed laser irradiation of a solid block of the implant material. In the present case a Nd:YAG laser is Q-switched with a Pockels cell, producing a 1 joule laser pulse with less than 0.1 microsecond length at a wavelength of 1.06 micron. The laser beam passes through steering prisms and vacuum system windows and is focused to a 2 mm diameter spot on the implant material by a 60 cm focal length lens. Tests thus far have utilized a solid boron target. This laser target is located in an electric field-free region, with the normal to its surface directed approximately toward the silicon wafer to be implanted. The laser beam strikes the surface from an angle of about 25° to the normal. The position and angle of the boron target are adjustable to optimize the intensity and uniformity of the ion beam in the direction of the silicon wafer, since these parameters are complicated functions of the laser beam energy and angle.^{8,9}

The result of the rapid deposition of laser energy on the implant material surface is to produce a high temperature plasma "bubble" of implant material ions and electrons, which "blow off" from the surface. In the present configuration this plasma bubble expands freely until it reaches the ion acceleration region. This distance is presently 37 cm. In the first measurements no acceleration was utilized, and the silicon wafers and an array of current measuring Faraday cups were placed at this position. This set-up allowed the measurement of implant ion fluence and areal uniformity. This configuration may prove to be valuable in its own right as a method for depositing a thin layer of certain materials for subsequent laser diffusion processing, since atoms of essentially any solid dopant can be deposited under

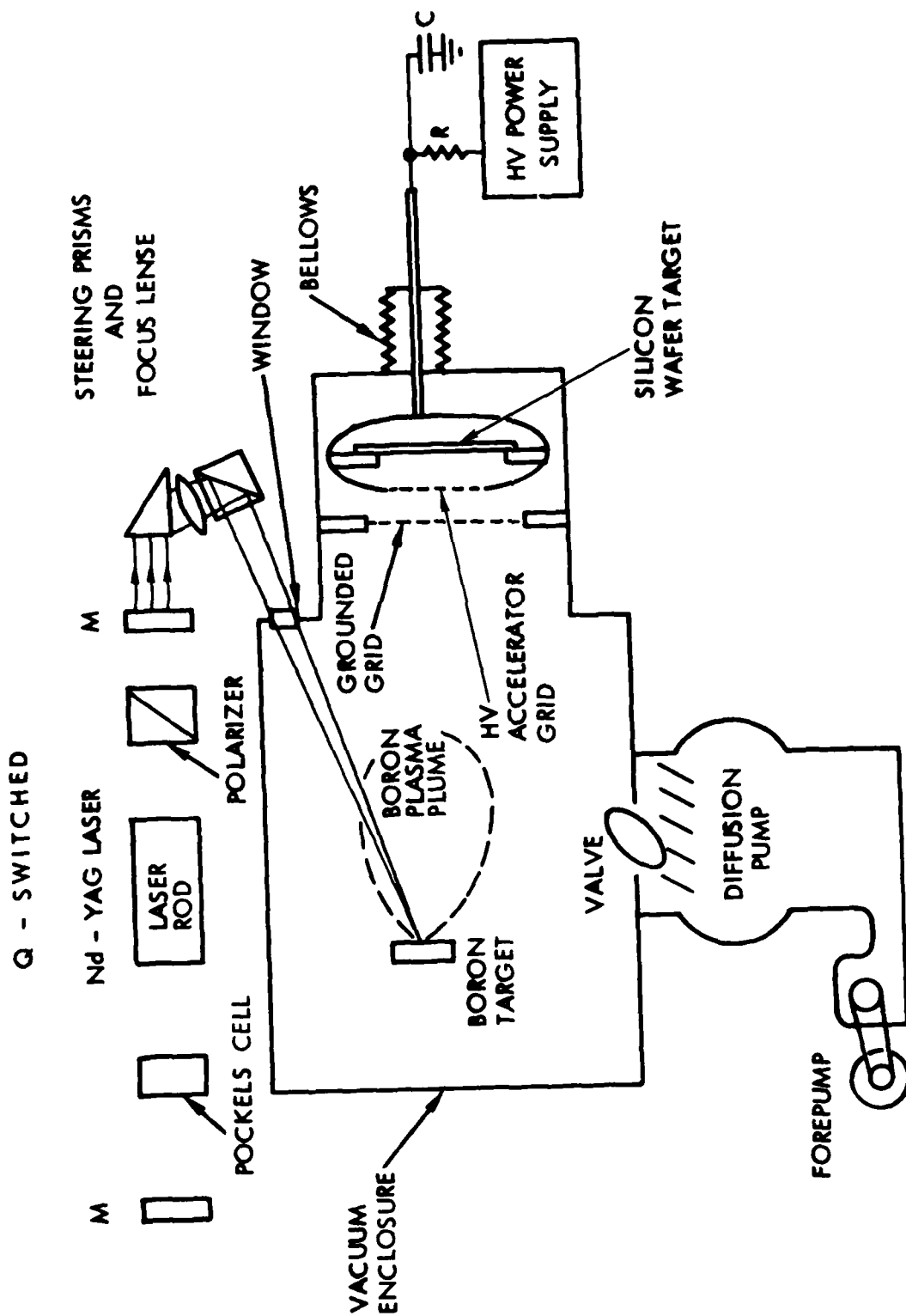


Figure 1a. Schematic Diagram of Laser Blow-Off Ion Implantation System

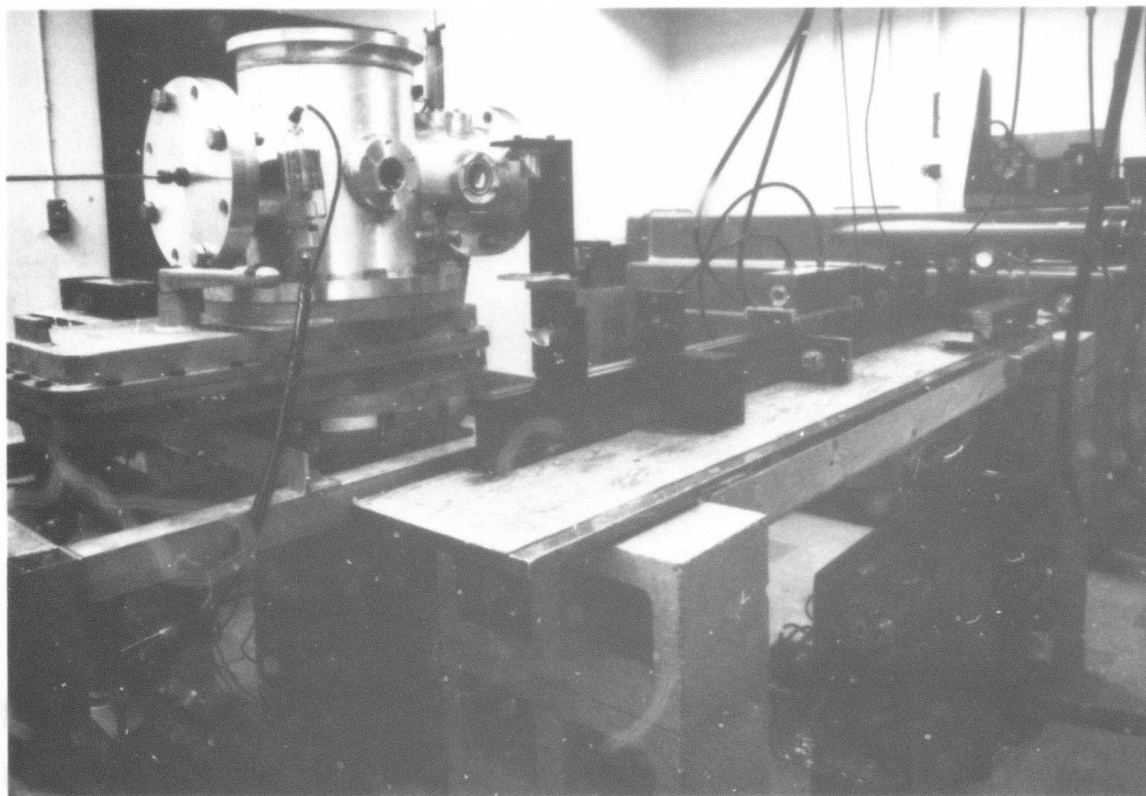


Figure 1b. Photograph of Laser Blow-Off
Ion Implantation System

vacuum conditions. The ion energies are a few hundred electron volts in this case, and thus barely penetrate the surface.

In the case where high energy implantation is to be used, acceleration of the implant ions is necessary as they reach the acceleration region. In the present configuration, this acceleration occurs between the grids shown. The first grid is held at the same potential as the field-free plasma expansion region. The second is held at a high negative voltage equal to the ion kinetic energy in eV desired. The silicon wafer is held at the same potential as the second grid at a distance approximately one centimeter beyond. This "drift" distance is intended to wash out any non-uniformity in implant caused by grid shadows or focusing effects. The drift distance cannot be too long because space charge spreading becomes severe because the plasma electrons are rejected by the ion acceleration region. The grids are presently 100 mesh stainless steel.

For initial tests, two types of silicon wafers were obtained from Monsanto. Both types are 3 inches in diameter and 0.015 inches thick, are oriented 100, and have resistivities of 10 ohm-centimeters. One type is N doped with phosphorus and the other type is P doped with boron. In order to economize on wafer material, the wafers are cut into cm-size chips for use when the measurements permit.

The accelerating voltage is supplied by a Plastic Capacitors Inc., 50 kV power supply, which charges an 0.05 microfarad capacitor across the accelerating grids. In the event of arc breakdown, the grids would have to dissipate 60 joules of energy. If an accelerating region area of 100 cm^2 and an implant ion density of $1 \text{ microcoulomb/cm}^2/\text{pulse}$ is considered, the accelerating voltage drops from 50 kV to 48 kV during the pulse. A larger capacitance value would reduce the voltage change, but the present value is safer during development.

The vacuum system consists of fairly standard components

including a 10 inch oil diffusion pump with water-cooled baffle and mechanical forepump. This system should be adequate for developmental purposes, but final definitive quantitative device tests may necessitate an ultra-high vacuum system to minimize surface contamination.

4.3 RESULTS

Measurements have been made and results obtained largely in the order of laser performance, implant plasma production, plasma plume characteristics, ion current and areal uniformity, implant material deposition without acceleration, and implant with high energy implant ions.

The Nd:YAG laser is operated at an output energy up to 1 joule per Q-switched pulse. This is lower than anticipated and appears to involve a problem with the polarizer and Pockels cell. The output energy also varies more from shot to shot than had been expected, about \pm 5 to 10 percent. This leads to a roughly similar variation in implant ion fluence from shot to shot. Although the laser energy and stability are less than might be desired, they should be sufficient to carry out the present tasks. So long as each ion pulse is monitored, and a number of shots are used per implant dose, it should be possible to control the total implant dose within the necessary limits. It was therefore decided to accept the laser performance as is for now, and move ahead with other aspects. It is certain that better laser performance is possible, and that eventually when high pulse repetition rates are needed a different laser will be necessary in any event.

A piece of pure, solid boron of dimension of order 1 cm was obtained for the laser blow-off target, that is, the source of implant ions. The actual purity is thought to be high, but this will be checked mass spectrometrically during analysis of the blow-off deposited material, as described below. Even with many laser shots, very little cratering of the boron occurred. This is consistent with earlier work, which indicated that less than one micron of material is removed per shot. No apparent difficulty was encountered in the implant ion plasma production.

In order to examine the characteristics of the expanding

plasma plume with regard to ion energy, current and number density, and angular distribution, an array of 5 Faraday cups was placed symmetrically along an arc perpendicular to the normal to the boron laser target in a plane containing the normal. The cups were 41 cm from the target and were spaced 4.2° apart with respect to the target, that is, the 5 cups observed the target at angles of 8.4° , 4.2° and 0° each side of the normal. The distance between centers of the outer cups was 12 cm. The Faraday cups detected ions within the expanding plasma plume as the ions reached the cup collectors. These cups were designed and tested for high current operation at the plasma densities encountered. The effective detection area was 1 cm^2 . These cups were of planar construction so that the ion transit time within the cup was negligibly small compared to the transit time from the laser target to the cup. Elements within the cup were electrically biased to suppress secondary electron emission. The Faraday cups could be operated in either the current sensing mode or the total charge collection mode, with the signals displayed directly on an oscilloscope in either case. The present results with boron ions are consistent with earlier theoretical and experimental work⁹ done in this laboratory on laser blow-off plumes. This work involved a model based on the following physical assumptions.

It was assumed that the deposited laser energy vaporizes and ionizes N_0 particles from a small region of the source material surface. This hot plasma "bubble" of N_0 ions begins to expand against the substrate and imparts momentum to it, thereby giving the center of mass of the N_0 ions a velocity v_{cm} in the laboratory coordinate frame. Because of symmetry, v_{cm} is normal to the surface. After the center of mass of the N_0 ions has moved a distance from the surface, the number density of ions remains high enough so that most of the N_0 ions equilibrate at a temperature T relative to their center of mass, which continues

to move at v_{cm} . That is, an observer moving with the center of mass would observe an essentially spherically symmetric plasma "bubble" in equilibrium at T , and freely expanding. As the number density continues to decrease, the ion velocity distribution corresponding to equilibrium at temperature T becomes "frozen" in the center-of-mass system. A laboratory observer at a larger distance from the source laser spot observes ions arriving with velocity essentially along a line from source spot to observer, but with a plume-like angular distribution due to the center-of-mass velocity v_{cm} superimposed on the purely thermal velocity distribution.

The theory thus consists simply of calculating the number density ρ and current density \vec{j} of ions to be observed in the laboratory frame resulting from N_0 ions expanding with spherical symmetry and having equilibrium velocity distribution corresponding to T in their center-of-mass system, and with a superimposed center-of-mass velocity v_{cm} .

Figure 2 shows the coordinate system for the theoretical model. The present adaptation differs in that a solid target is struck by the laser beam on the front surface. The current density of ions \vec{j} in ions per unit area per unit time is given by

$$\vec{j}(r, \theta, \lambda, \eta) = \left(\frac{512}{9} \right) \left(\frac{2}{\pi} \right)^{3/2} \left(\frac{kT}{m} \right)^{1/2} \frac{N_0}{r^3} \exp \left(-\frac{3\lambda^2}{2} \right) \cdot (\phi\eta)^{-4} \\ \times \exp \left\{ \left[-\frac{32}{3} (\phi\eta)^{-2} \right] \left[1 - 3(\lambda \cos \theta)(\phi\eta)/4 \right] \right\} \hat{r}$$

where

$$\phi = \left\{ \sqrt{(\lambda \cos \theta)^2 + \frac{16}{3}} - (\lambda \cos \theta) \right\} ,$$

$$t_{max} = 3/8 \phi \sqrt{m/3kT} \quad r ,$$

$$\eta = t/t_{max} ,$$

and

$$\lambda v_{RMS} = v_{cm} = \lambda \sqrt{3kT/m}$$

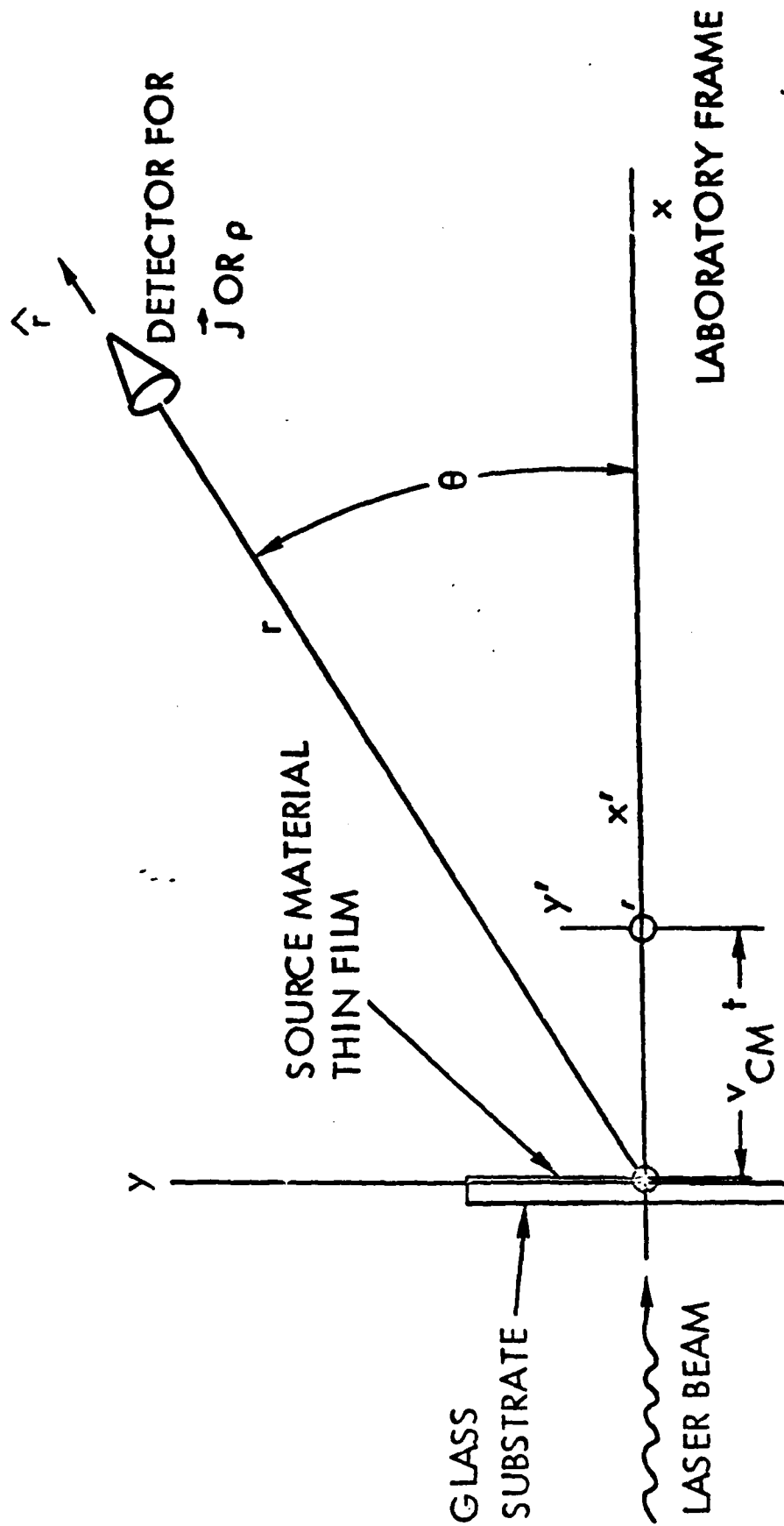


Figure 2. Geometric Arrangement for the Theoretical Model and Experiment

gives the relation defining the "blow-off" parameter λ . Small λ implies small v_{cm} and hence a broad angular distribution, while large λ implies a narrow "plume". The other parameters above include time t , ion mass m , Boltzmann's constant k , temperature T , and time of J_{max} , t_{max} . Figure 3 shows these results graphically in terms of J/J_{max} versus η , and therefore represents an expected picture of \dot{j} versus t on an oscilloscope trace of a current sensing Faraday cup. Picture A of Figure 4 shows an actual trace of a boron ion pulse from the present measurement. The points on Figure 3 are the same data plotted there. The skewness away from the theoretical curves has been noted before⁹ for ions, while the agreement is quite good for neutral atom blow-off.⁹ The λ values depend on laser energy density and the target materials, and are thus subject to some control. The general agreement with theory is sufficiently good to predict currents and densities as functions of time, distance and angles. Of particular importance is the sensitivity of the angular distribution to λ , as seen next. The total number of ions passing across unit area normal to \hat{r} per pulse is given by

$$\int_0^{\infty} \dot{j} dt = \frac{N_0}{4\pi r^2} \frac{2}{\sqrt{\pi}} \exp(-3\lambda^2/2) \\ \times \left[\chi + \sqrt{\pi}(1/2 + \chi^2)(1 + \operatorname{erf} \chi) e^{\chi^2} \right] \hat{r}$$

where

$$\chi = \sqrt{3/2} (\lambda \cos \theta)$$

and

$$\operatorname{erf} \chi = \frac{2}{\sqrt{\pi}} \int_0^{\chi} \exp(-u^2) du$$

Figure 5 shows these theoretical angular distributions as functions of λ . Also included are previous experimental points obtained for aluminum ions and present points obtained for boron ions.

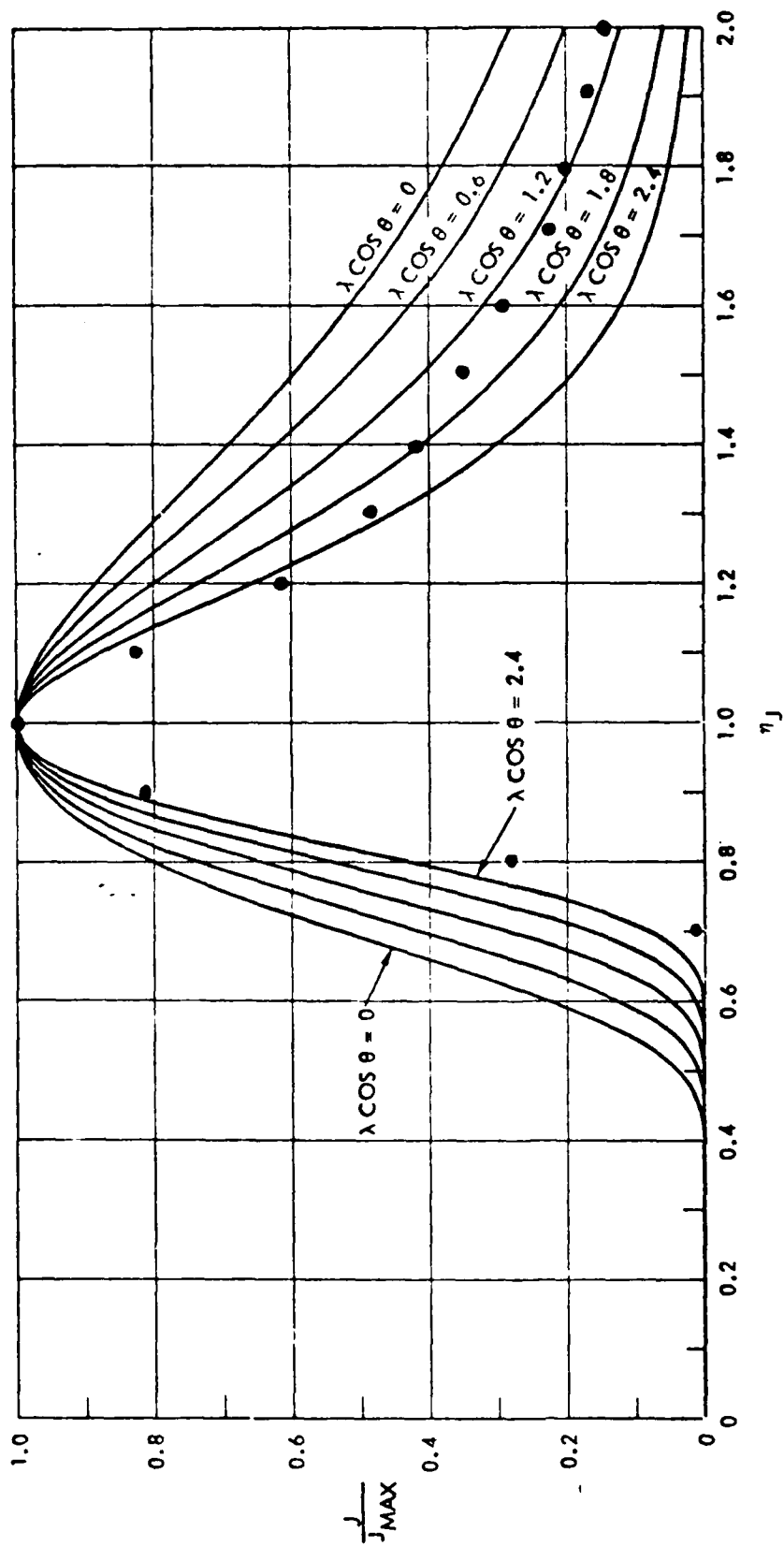
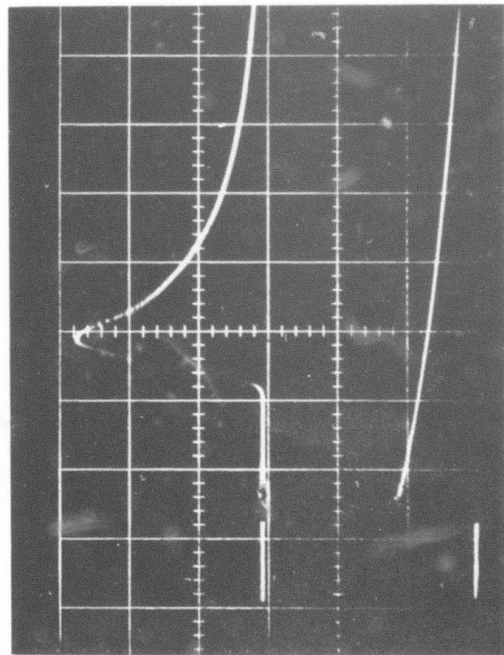
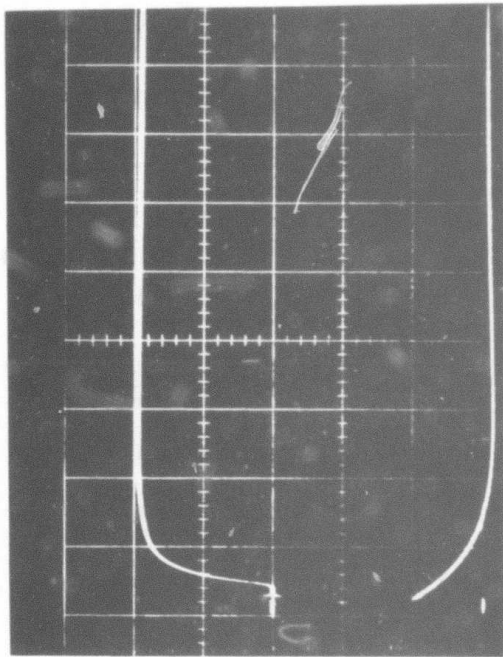


Figure 3. Theoretical Curves for Beam Particle Current Density j versus Time, Normalized to the Time at Which j is a Maximum. Points are measured values for boron ions. Boron ion current vs time



(a)

Upper: Boron Ion Current vs Time
Lower: Laser Energy and Timing Marker
2 μsec /large div



(b)

Upper: Boron Ion Collected Charge vs Time
Lower: Laser Energy and Timing Marker
20 μsec /large div

Figure 4. Unaccelerated Boron Ion Pulses

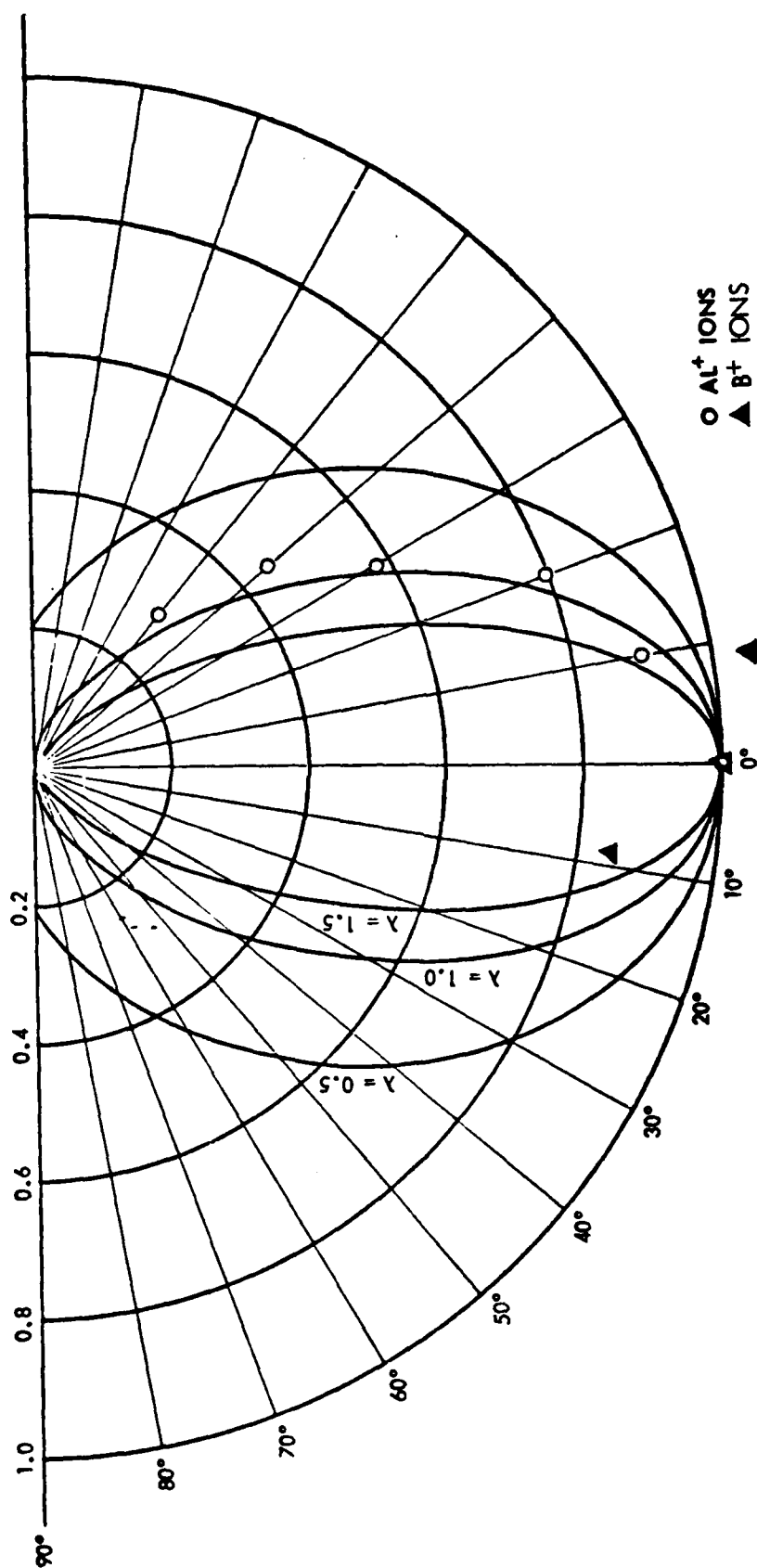


Figure 5. Theoretical Curves for $\int_0^\infty j dt$ versus Detector Angle θ at Constant Distance r and Normalized to the Value for $\theta = 0$. Points are measured values for aluminum and boron ions.

It is obvious that small values of λ are necessary if one is to implant large areas with high uniformity without "rastering" the wafer between shots. The ion arrival time profiles may also be very important in self-annealing aspects, since the thermal pulse will reflect the arrival time pulse. Figures 4 and 5 from Reference 8 show examples of widely differing angular distributions depending on laser beam conditions. The presently obtained angular distributions are adequate for present purposes and will be optimized further, but it is clear that variations in ion fluence as a function of angle put eventual limits on the size of wafers which can be implanted with high uniformity over the surface.

Measurements have been made to determine the actual ion current and areal implant ion density by combining Faraday cup array current measurements with implant ion deposition without acceleration. The currents and charge collected are displayed directly on an oscilloscope for the two outer and the middle Faraday cups in the array. The apertures of the other two cups are covered with silicon wafer chips. A number of laser shots are then made to deposit boron on the silicon chips, at the same time summing the charge collected on either side of the chips. Table 1 shows the results of one such run. In this particular case, cup A was on the side of the normal toward the laser beam, and the results show the asymmetry toward the laser beam which was reported earlier.⁸ The uniformity of $\pm 2\%$ over the 3 cm interval between cups A and M is acceptable for now, but the $\pm 8\%$ variation between cups B and M is not. This run shows a particular strong dependence on angle, a dependence itself dependent on laser conditions as noted above.

The silicon chips deposited with boron in runs like Table 1 were analyzed on an Applied Research Laboratories IMMA (Ion Microprobe Mass Analyzer). A schematic diagram of this instrument is shown as Figure 6. It has been used extensively in early work

Table 1. Boron on Silicon Experimental Results

SHOT NUMBER	RELATIVE LASER ENERGY	CHARGE COLLECTED (MICROCOULOMRS)		
		CUP A	CUP M	CUP B
1	13.1	OFF SCREEN (~1.05)	.98	.80
2	9.9	.98	.92	.79
3	8.5	.79	.77	.67
4	8.6	.75	.73	.63
5	8.4	.78 <u><u>4.35</u></u>	.75 <u><u>4.15</u></u>	.65 <u><u>3.54</u></u>

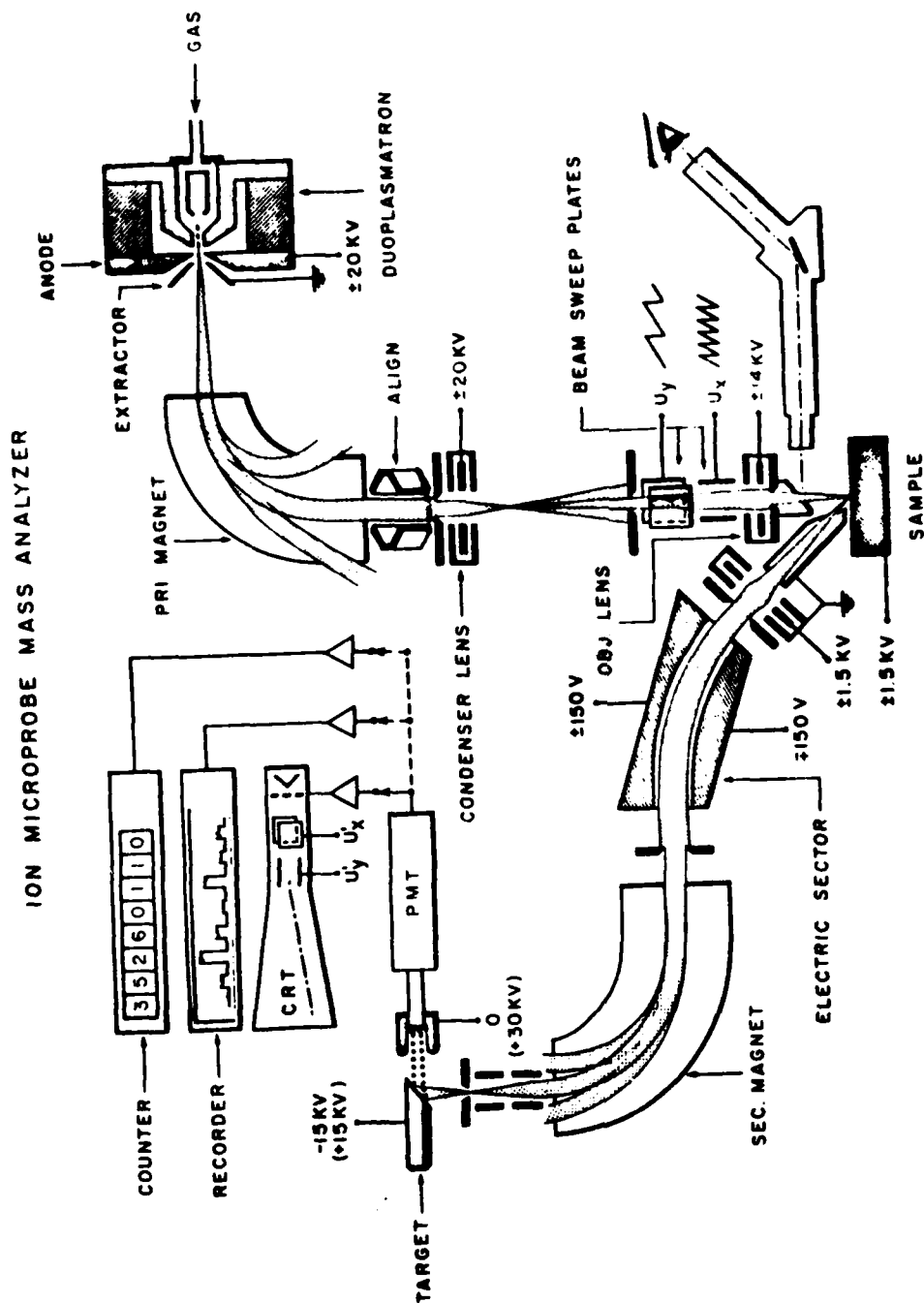


Figure 6. Applied Research Laboratories IMMA
(Ion Microprobe Mass Analyzer)

in order to determine implant uniformity, purity, and depth profiles. Actual semiconductor device implants will of course be necessary to prove the effectiveness of the blow-off implant method in the final analysis.

Figure 7 shows the depth profile of a boron implant into a 3-inch diameter silicon wafer, with an implant ion energy of 40 KeV. One hundred laser shots were employed, and the ion fluence was a few times 10^{12} boron ions per cm^2 per laser shot. The depth profile measurements can be made absolute by calibrating the IMMA against a known profile produced by conventional ion implantation techniques.

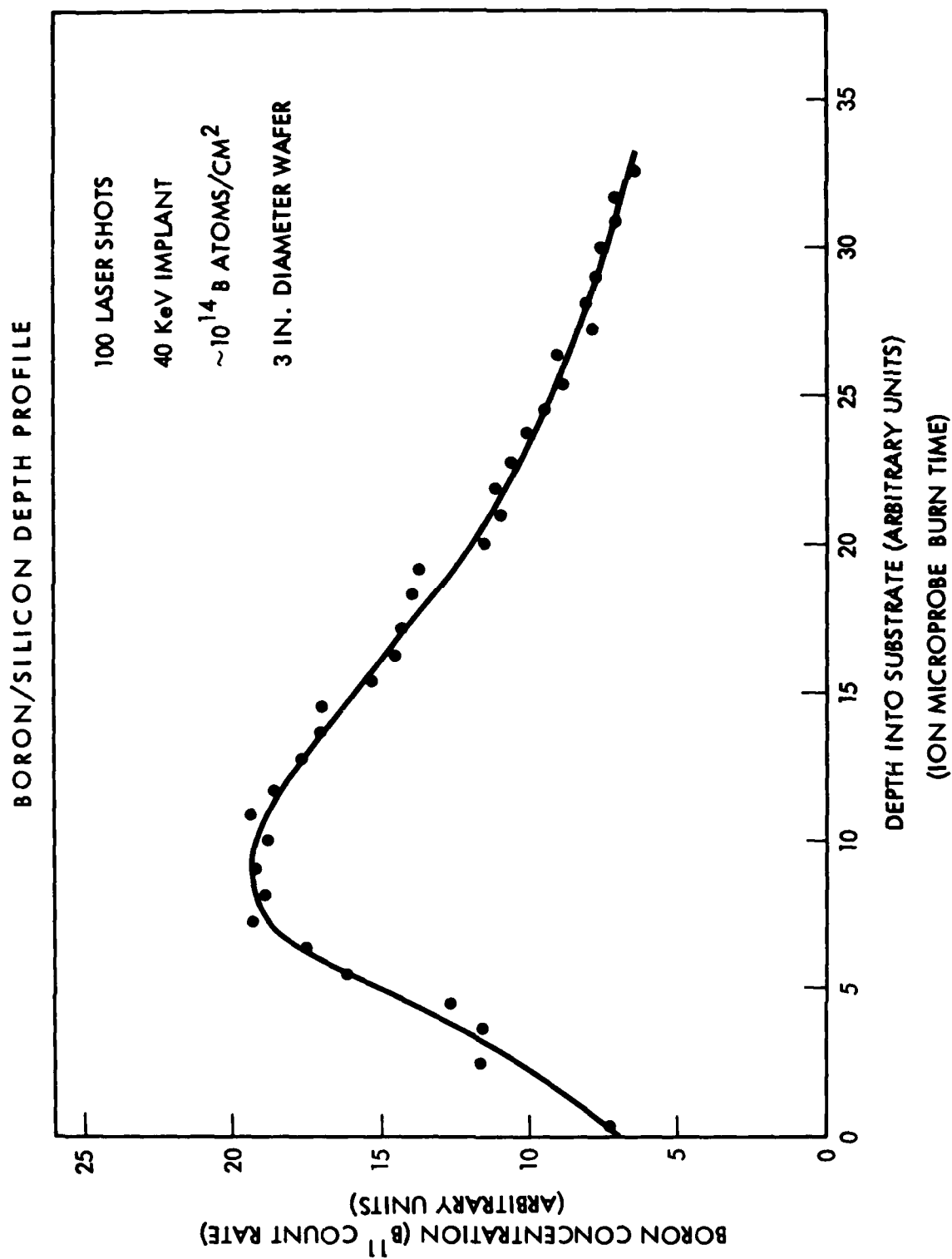


Figure 7. Boron/Silicon Depth Profile

REFERENCES

1. J. Z. Wilcox, "The Effect of Carrier Diffusion on Laser Heating of Lightly Damaged Semiconductors," submitted to J. Appl. Phys., 1979.
2. S. Prussin and W. von der Ohe, "Laser Annealing of Low Fluence Ion-Implanted Silicon," submitted to J. Appl. Phys., 1979.
3. For a review article and further reference, see C. W. White, J. Narayan, and R. T. Young, "Laser Annealing of Ion-Implanted Semiconductors," Science 204, (4 May 1977), 461.
4. R. Bacri, et al., "Arsenic Diffusion in Silicon Melted by High-Power Nanosecond Laser Pulsing," Appl. Phys. Letters, 33, No. 2 (1978), 137.
5. D. H. Auston, et al., "Time-Resolved Reflectivity of Ion-Implanted Silicon During Laser Annealing," Appl. Phys. Letters, 33, No. 5 (1978), 437.
6. J. C. Muller, et al., "Laser Beam Annealing of Heavily Doped Implanted Layers on Silicon," Appl. Phys. Letters, 33 (1978), 287.
7. A. Gat, et al., "Physical and Electrical Properties of Laser-Annealed Ion-Implanted Silicon," Appl. Phys. Letters, 32, No. 5 (1978), 276.
8. J. F. Friichtenicht, N. G. Utterback, and J. R. Valles, "Intense Accelerated Metal Ion Beam Utilizing Laser Blow-Off," Rev. Sci. Instru., 47, (1976), 1489.
9. N. G. Utterback, S. P. Tang, and J. F. Friichtenicht, "Atomic and Ionic Beam Source Utilizing Pulsed Laser Blow-Off," Physics of Fluids, 19, (1976), 900.

APPENDIX A

THE EFFECT OF CARRIER DIFFUSION ON LASER-HEATING OF LIGHTLY DAMAGED SEMICONDUCTORS*

J. Z. WILCOX

TRW Defense and Space Systems Group, Redondo Beach, California 90278

ABSTRACT

It has been observed that the surface temperature obtained during laser heating of lightly damaged material is generally considerably lower than the temperature obtained in heavily damaged material. We develop a model which explains this observation by taking into account the diffusion of the photoexcited carriers. The time evolution of temperature profiles was calculated for pulsed ruby and Nd:YAG illumination of silicon, and ruby illumination of GaAs. The material, optical, and

* Supported in part by DARPA Contract MDA903-78-C-0284.

electronic properties were varied, according to the material quality. Surface recombination of the carriers was also taken into account. For the same laser power, the induced temperature was lower and the heating times were longer in good quality materials than in heavily damaged materials. This is because of longer carrier diffusion lengths in good quality material. The effect of the damage on the heating was found to be much more pronounced for Nd:YAG than for ruby irradiation because a larger portion of the ruby laser energy (excess above bandgap) is given rapidly to the lattice through quasi-thermalization inside the semiconductor energy bands. Thermal spikes are formed as the result of the preferential recombination of the carriers at the surface. For a sufficiently fast surface recombination, the temperature profile may develop a secondary maximum in the material interior.

I. INTRODUCTION

There is considerable interest in the use of lasers for processing of semiconductor surfaces.¹ The majority of experiments has been in pulsed laser annealing of comparatively high-dose implantations. In these experiments, the resulting activated dopant concentrations were often in excess of the limits of equilibrium solid solubility, and the shapes of the ion-implanted profiles were changed as a result of the illumination.² This led to the suggestion that the near-surface regions of the irradiated material actually melted and underwent a type of liquid epitaxy in these experiments. The suggested model is strongly supported by numerical results of several model calculations.³

Heavily damaged material has been successfully annealed also with scanned cw Nd:YAG lasers.⁴ No significant dopant redistribution was observed after the annealing, indicating that the regrowth was through solid state epitaxy. This was made possible because of the long times involved in these experiments. Nd:YAG laser annealing was found to be a very sensitive function of the dose of the implanted impurities.

Laser-induced annealing of lightly damaged material has received much less attention. We have studied⁵ the use of Q-switched ruby lasers for activation of low fluence non-amorphous silicon and neutron-transmuted silicon, and found that powers required for activation of non-amorphous surfaces were much larger than those required for amorphous surfaces. The required powers depended strongly on the dose of implanted impurities. For the neutron-transmuted silicon, an energy density of 4 J/cm^2 was not effective for activation, unless additional damage such as Ne implantation was introduced into the material. Lightly implanted wafers showed remelted spots at the surface, while none was observed at surfaces of amorphized

layers. The results of these experiments could not be explained in terms of a weaker optical absorption in crystalline silicon alone.

The present work addresses the difference between laser-induced heating of heavily and lightly damaged materials. It presents the results of the thermal calculations which take into account the diffusion of the photoexcited carriers. Previous thermal models have been concerned with heavily damaged materials, in that they assumed that the absorbed optical energy is converted to heat in the immediate vicinity of the absorbed photons. However, in strongly absorbing semiconductors, the primary effect of the absorbed radiation is to generate carriers. Heat is generated when the carriers recombine, i.e., after they have diffused a distance on the order of carrier diffusion length. In good quality materials, the diffusion lengths may be longer than the optical absorption depth. Hence, the carrier diffusion enlarges the heating volume, and, for the same laser power, causes the surface temperature in lightly damaged material to be lower than in heavily damaged material. Furthermore, a large number of carriers will reach, and recombine at, the surface, making it qualitatively feasible to melt surface defects in lightly damaged materials.

The conversion of optical energy to heat consists of two major steps:

- (i) absorption of laser light, and
- (ii) conversion of absorbed optical energy to heat.

We consider strongly absorbing semiconductors. In strongly absorbing semiconductors, the dominant⁶ absorption mechanism at frequencies higher than the bandgap frequency is interband transitions. The conversion of absorbed energy to heat is accomplished through thermalization of photoexcited carriers. Once the conversion has been accomplished, the temperature distribution is determined by solving the thermal diffusion

equation in the semiconductor. At issue is the proper representation of the source term in the heat equation.

In the model used in this work, we categorize the thermalization as consisting essentially of two steps, operative either in parallel or in sequence: relaxation of the electron "excess" energy (above the bandgap), and relaxation of the bandgap portion of the energy. This categorization is convenient because the electron redistribution inside the conduction band proceeds generally at a different rate than the electron-hole recombination across the semiconductor bandgap. The bandgap portion of the electron energy is released to heat at the rate $\approx E_g \Delta n \tau^{-1}$, where τ is the carrier lifetime, E_g is the semiconductor bandgap, and $\Delta n = \Delta n(x,t)$ is concentration of the photoexcited carriers. Δn is calculated by solving the electron diffusion equation. Thus, the bandgap portion of the electron energy is released into a volume bounded by a depth equal to $\max(L, \alpha^{-1})$, where $L = \sqrt{D\tau}$, D is carrier diffusivity and α is optical absorption coefficient.

The conversion of the excess portion of the electron energy is assumed in this work to be instantaneous. This is because the characteristic "quasi-thermalization" frequency is on the order of the lattice vibrational frequency, $f_c \approx 10^{12} - 10^{13} \text{ sec}^{-1}$, which is much faster than any other rate in the problem.⁷

The presence of defects and interfaces also affects the heating profiles. Interfaces affect heating mainly because of surface recombination of the photoexcited carriers. The effect of the surface will be taken into account in this work through the surface recombination velocity v_s .

Bulk defects may be categorized as localized or distributed. Both affect optical absorption as well as carrier diffusion. The influence of the distributed defects will be taken into account in that the values of the optical absorption coefficient, carrier lifetime, and diffusivity will be different for heavily damaged than for good quality materials. However, the crystal will be considered homogeneous, and its properties independent of time. In this sense, the values of the material parameters used are some "average" values of the parameters during the processing. The main reason for this is mathematical simplicity. The localized bulk defects will not be treated here explicitly. However, their effect on the heating should be similar to that of the surface defects. This is because both surface and localized defects are fast recombination centers, with the subsequent release of the carrier energy. This leads to the formation of thermal spikes at, and a possible dissolution of, localized defects.

As has already been mentioned, the "bandgap energy source term" in the heat equation requires knowledge of the electron concentration, $n(x,t)$. For constant τ , D , and v_s , we have solved the electron diffusion equation exactly for a square-shape laser pulse (no drift current). The solution for $n(x,t)$ is a closed-form expression consisting of complementary error functions. To the best of our knowledge, this solution has never before been reported in the literature. The existence of a closed-form expression for $n(x,t)$ is important for our purposes since it avoids numerical integration of the electron diffusion equation. The heat transport equation is then solved numerically, with the temperature dependence of the thermal conductivity included.

In Section II of this paper, we describe the mathematical basis of the model. In Section III, we discuss the results of the numerical computations of the temperature. Section IV summarizes the results.

II. MODEL

The photon-to-thermal energy conversion consists of photoexcitation and thermalization of the photoexcited carriers, and heat transport.

A. Concentration of Photogenerated Carriers

The instantaneous concentration of the photogenerated carriers is, in the one-dimensional approximation, and in the absence of electric fields, obtained by solving the electron transport equation,

$$\frac{\partial n}{\partial t} = g - \frac{\Delta n}{\tau} + D \frac{\partial^2 n}{\partial x^2}, \quad (1)$$

where the generation function g gives the photogeneration rate of the carriers,

$$g = \alpha N e^{-\alpha x}, \quad (2)$$

where α is the optical absorption coefficient, and $N = N(t)$ is the photon flux incident at the surface. $N(t) = F(t)/h\nu$, where $F(t)$ is the absorbed laser power and $h\nu$ is the photon energy.

$$\Delta n \equiv n(x,t) - n_0, \quad (3)$$

where n_0 is the equilibrium concentration, τ and D are minority carrier lifetimes and diffusion constant, respectively.

In Equation (1), α , τ , and D are, in general, functions of both x and t . The x -dependence arises due to the spatial inhomogeneities in the semiconductor; the time dependence arises from the dependence of α , D , and τ on temperature. Additional time dependence arises due to changes in the

semiconductor properties as the damage disappears during the annealing. For high carrier concentrations, α may be a function of the photocarrier concentration $n(x,t)$. It would be quite complicated to fully account for the effect of the changing material properties. We approximate material properties by some "average" values and the crystal is assumed homogeneous, with the exception of the front surface.

Taking into account surface recombination of the carriers, the boundary conditions are

$$j(x = 0, t) = -D \left. \frac{\partial n}{\partial x} \right|_{x=0} = -v_s (n(0) - n_0) \quad (4)$$

and

$$n(x = \ell) = n_0, \quad (5)$$

where v_s is the surface recombination velocity and ℓ is the semiconductor thickness. Equations (4) and (5) correspond to a finite flux of carriers at the semiconductor front surface, and a constant carrier concentration at the slab back boundary. The initial condition is

$$n(x, t = 0) = n_0. \quad (6)$$

In general, if N , α , τ , and D are functions of x and t , Equation (1) has to be solved numerically. However, Equation (1) can be solved exactly analytically for the special case when α , τ , and D are constants, and the generation function $N(t)$ is a square-shaped laser pulse,

$$\begin{aligned} N(t) &= N_0 & 0 < t < t_p, \\ N(t) &= 0 & \text{otherwise} \end{aligned} \quad (7)$$

In Eq. (5), t_p is the length of the laser pulse and N_0 is the number (constant) of arriving photons at the semiconductor front surface. The mathematical methods are discussed in Appendix I. The result is

$$\begin{aligned} \Delta n(x, t) = & \frac{\alpha N_0 \tau}{2(1 - L^2 \alpha^2)} \left\{ \sum_{(+, -)} \frac{1 + \frac{\alpha D}{v_s}}{1 - \frac{L}{v_s \tau}} e^{\pm \frac{x}{L}} \operatorname{erf} \left(\pm \frac{x}{\sqrt{4Dt'}} + \sqrt{\frac{t'}{\tau}} \right) \right. \\ & + \sum_{(+, -)} \frac{\left(1 + \frac{D\alpha}{v_s} \right)}{\left(1 - \frac{D\alpha}{v_s} \right)} \exp \left[\pm \alpha x - \frac{t'}{\tau} (1 - \alpha^2 L^2) \right] \operatorname{erfc} \left(\pm \frac{x}{\sqrt{4Dt'}} + \alpha \sqrt{Dt'} \right) \\ & \left. + \frac{2(1 - L^2 \alpha^2)}{\left(\frac{\alpha D}{v_s} - 1 \right) \left(1 - \frac{v_s}{D} \right)} \exp \left[- \frac{t'}{\tau} + (t' v_s + x) \frac{v_s}{D} \right] \operatorname{erfc} \left(v_s \sqrt{\frac{t'}{D}} + \frac{x}{\sqrt{4Dt'}} \right) \right\}_{t_0}^t \end{aligned} \quad (8)$$

where $t_0 = \max(0, t - t_p)$, the diffusion length $L = \sqrt{D\tau}$, and $\operatorname{erf}(z)$ and $\operatorname{erfc}(z)$ are error and complementary error functions, respectively.

Equation (8) is evaluated between the indicated upper and lower boundaries, t and t_0 , respectively.

The importance of the existence of solution (8) for our purposes derives from eliminating the need for numerical integration of Eq. (1). $n(x, t)$ appears as a source term in the thermal diffusion equation discussed in the next section.

B. Thermal Transport

The temperature distribution in the semiconductor after the application of the laser pulse is obtained by solving the thermal equations,

$$\frac{\partial T}{\partial t} - \frac{\partial}{\partial x} \left(\frac{\kappa}{c_p} \frac{\partial T}{\partial x} \right) = \frac{S(x,t)}{c_p}, \quad (9)$$

where c_p and κ are the specific heat and thermal conductivity, respectively, and where the source function S is the heat flux deposited in the semiconductor lattice per unit length. Equation (9) is solved subject to appropriate boundary conditions. In many instances, these are (i) initial temperature, (ii) thermal flux at the front surface, and (iii) thermal flux or temperature of the heat sink at the back of the sample.

(1) Lightly Damaged Materials

Following our previous discussion, we express S as a summation of three terms, S_1 , S_2 and S_3 . S_1 is the "excess" portion of the electron energy, S_2 is the bandgap portion of the electron energy, and S_3 is energy released by carriers recombined at the semiconductor surface.

The excess portion of the electron energy is released during quasi-thermalization of photoexcited electrons inside the conduction band. Since the characteristic frequency, $10^{12} - 10^{13} \text{ sec}^{-1}$ is much faster⁷ than any other rate in the problem, we approximate

$$S_1(x,t) = (h\nu - E_g)\alpha N(t)e^{-\alpha x}, \quad (10)$$

where ν is the laser frequency and E_g is the bandgap energy.

The bandgap portion of the electron energy is transferred to heat at rate τ_0^{-1} , where τ_0 is the nonradiative lifetime of the electron,

$$S_2(x,t) = E_g \frac{(n(x,t) - n_0)}{\tau_0} \quad (11)$$

The surface recombination contributes a term

$$S_3(x,t) = E_g v_s (n(x,t) - n_0) \delta(x) \quad (12)$$

where $\delta(x)$ is the delta function. Mathematically, the effect of $S_3(x,t)$ will be to introduce a finite derivative $\partial T / \partial x$ at $x = 0$; see Eq. (14) in what follows.

Similarly as for the electron diffusion, we consider an essentially uniform crystal. It is worth noticing, however, that the effect of the presence of localized carrier "sinks" in the crystal on temperature could be included through source terms of the type of Eq. (12) (which in turn introduce discontinuities in $\partial T / \partial x$). Physically, this corresponds to a localized deposition of the energy, and a subsequent formation of thermal spikes at defect sites. This makes dissolution of localized defects feasible. In this sense, location $x = 0$ of this paper may be viewed as a defect site, with the recombination rate for the carriers equal to $v_s \Delta n(x,t) \delta(x)$.

Neglecting loss of heat irradiated from the front surface (it has been estimated to be typically six orders of magnitude smaller than the incoming laser flux), Eq. (9) is then solved subject to the following initial and boundary conditions:

$$T(x, t = 0) = T_0 \quad (13)$$

$$\frac{\partial T(x = 0, t)}{\partial x} = - \frac{E_g}{\kappa} v_s (n(0, t) - n_0) \quad (14)$$

$$T(x = \ell, t) = T_0 \quad (15)$$

where T_0 is the temperature of the heat sink at the back of the sample. Equation (14) was obtained by substituting Eq. (12) into Eq. (9) and integrating the

resulting equation across the front boundary. Equation (9) has to be solved numerically.

(2) Heavily Damaged Materials and $\kappa, c_p = \text{Constants}$

For heavily damaged materials and $\kappa, c_p = \text{constants}$, Eq. (9) has a closed-form solution. This is because for extremely short carrier lifetimes, $\tau v_s \alpha < 1$ and $\tau D \alpha^2 < 1$ (i.e., bulk recombination is faster than either the surface recombination or carrier diffusion), the source functions simplify to

$$S_2(x, t) \equiv E_g \frac{(n(x, t) - n_0)}{\tau} \approx E_g g = E_g \alpha F(t) e^{-\alpha x} \quad (16)$$

and

$$S_3(x, t) \approx 0 \quad (17)$$

This yields the source term

$$S \equiv S_1 + S_2 = h\nu \alpha N(t) e^{-\alpha x} \quad (18)$$

and the boundary condition

$$\frac{\partial T(x=0, t)}{\partial x} = 0 \quad (19)$$

The solution to Eq. (9) is then obtained by taking the limit $1/\tau \rightarrow 0$ in Eq. (A.10) of Appendix (A.2). This yields

$$\Delta T(x, t) = \frac{F_0}{2\alpha\kappa} \left\{ e^{\frac{\kappa}{c_p} \alpha^2 t'} \sum_{(+, -)} e^{\pm \alpha x} \operatorname{erfc} \left(\alpha \sqrt{\frac{\kappa t'}{c_p}} \pm \frac{x}{\sqrt{(4\kappa/c_p) t'}} \right) + 4\alpha \sqrt{\frac{\kappa t'}{c_p \pi}} \exp \left[\frac{-x^2}{(4\kappa/c_p) t'} \right] + 2\alpha x \operatorname{erf} \left(\frac{x}{\sqrt{(4\kappa/c_p) t'}} \right) \right\}_{t_0}^t \quad (20)$$

where $F_0 \equiv h\nu N_0$, and the upper and lower boundaries are $t' = t$ and $t_0 = \max(0, t - t_p)$, respectively.

III. NUMERICAL RESULTS

Equation (9) was solved numerically for ruby and Nd:YAG lasers, GaAs and silicon, and various values of laser and material parameters. The values of the material parameters ranged from those appropriate for heavily damaged materials to those corresponding to high-quality materials. The specific heat was taken as constant, $c_p \approx 1.6 \text{ J/cm}^3$ for Si and $c_p \approx 1.78 \text{ J/cm}^3$ for GaAs. The thermal conductivity $\kappa(T)$ was represented by a summation of exponentials chosen to fit data measured for pure GaAs and silicon.⁸ High impurity concentrations tend to lower these values; this was not taken into account. The carrier lifetimes were taken $\tau = \tau_0$.

The laser pulse lengths were taken to be 10 nsec for ruby, and 100 nsec for Nd:YAG laser (these are the optimum lengths for heavily damaged materials). For GaAs, the optical absorption coefficient (ruby only) was $\alpha = 2 \times 10^4 \text{ cm}^{-1}$. The optical absorption coefficient for ruby irradiation was $\alpha = 2 \times 10^3 \text{ cm}^{-1}$ and $2 \times 10^4 \text{ cm}^{-1}$ for crystalline and amorphous silicon, respectively. For Nd:YAG irradiation, α was taken as $\alpha \approx 10^3 \text{ cm}^{-1}$ for amorphous and heavily damaged, $\alpha \approx 500 \text{ cm}^{-1}$ for lightly damaged, and $\alpha \approx 100 \text{ cm}^{-1}$ for good quality silicon.⁹ The values of D and τ ranged from $30 \text{ cm}^2 \text{ s}^{-1}$ to $3 \text{ cm}^2 \text{ s}^{-1}$, and 10^{-5} sec to 10^{-10} sec , respectively, for silicon, and from $200 \text{ cm}^2 \text{ s}^{-1}$ to $15 \text{ cm}^2 \text{ s}^{-1}$ and 10^{-8} sec to 10^{-11} sec , respectively, for GaAs. The surface recombination velocity was $v_s = 2 \times 10^7 \text{ cm s}^{-1}$, $2 \times 10^4 \text{ cm s}^{-1}$, and 0.

Samples of the numerical results are shown in Figures 1-12. The profiles are shown as a function of the normalized distance αx away from the semiconductor front surface, with time (in fractions and multiples of the pulse length t_p) as a parameter. The symbols shown (in cgs units

unless specified otherwise) have their usual meaning. The normalized temperature $(T-T_0)/(F_0/\kappa_0\alpha)$ is dimensionless, κ_0 is a quantity (equal to one) which has the dimension of thermal conductivity. F_0 is the actual absorbed power (in W/cm^2). Most of the profiles shown correspond to $\Delta T_{\max} \approx 900 - 1,400^\circ\text{C}$ (the exact number can be calculated from parameters specified in each figure). Before inspecting the profiles, it is convenient to qualitatively summarize the main results of these calculations. This will aid understanding when inspecting the profiles.

A. Heavily Damaged Materials

For heavily damaged materials, the effects of carrier diffusion and surface recombination on heat generation can be neglected. The simulated profiles approached those calculated using Eq. (20) (Eq. (20) assumes $\kappa = \text{constant}$, $\tau v_s D < 1$ and $\tau D \alpha^2 < 1$). As compared to Eq. (20), the effect of $\kappa \approx \kappa(T)$ on the profiles was to slightly increase the surface temperature, and narrow the profile width. This is because $\kappa(T)$ decreases with temperature increasing.

Surface Temperature and Profile Width: For the pulse length shorter than the thermal diffusion time, $t_p < t_{th}$, where $t_{th} = c_p/\kappa\alpha^2$, the profiles are optical absorption depth-limited. The profile width $\approx \alpha^{-1}$, and ΔT_{\max} grows linearly with both the pulse length and optical absorption coefficient, $\Delta T_{\max} \approx F_0 t_p \alpha / c_p$. For the pulse length longer than t_{th} , $t_p > t_{th}$, the profile is thermal diffusion-limited. Its width is $\approx (\kappa t_p / c_p)^{1/2}$, and ΔT_{\max} is independent of α and proportional to the square root of the pulse length, $\Delta T_{\max} \approx F_0 \sqrt{t_p / \kappa c_p}$ (the surface temperature approaches saturation for extremely long pulses). In either case, ΔT_{\max} is approximately linear with pulse peak power (ΔT_{\max} is exactly linear with F_0 for $\kappa = \text{constant}$). The heating is most efficient (least laser energy required) when $t_p \approx t_{th}$.

The optical depth-limited profiles are generally narrower than the thermal diffusion-limited profiles.

Temperature Decay: After the end of the laser pulse, the temperature drops and the profile broadens as the heat propagates into the bulk. The decay is much faster for strong absorption than for weak absorption. This is because the thermal diffusion time $c_p/\kappa\alpha^2$ is much longer for small α than for large α . For example, for $\alpha = 2 \times 10^3 \text{ cm}^{-1}$, the surface temperature typically dropped to one-half (1/2) of its maximum value at $t \approx 100 t_p$. For $\alpha = 2 \times 10^4 \text{ cm}^{-1}$, the halftime was only $t \approx 5 t_p$.

For comparison purposes, Eq. (9) was, for heavily damaged materials, also solved for the "Gaussian" pulse shapes. We have observed really no significant difference between the shapes of the thermal profiles created by square and Gaussian pulse shapes. The resulting temperature distributions were affected much more by the condition α^{-1} vs. $\sqrt{\kappa t_p/c_p}$, than by the pulse shape. For the Gaussian pulse, slightly higher laser powers were required to achieve the same surface temperature as for the square-shape pulse. The Gaussian profiles tend to decay more slowly than the square-shaped pulse profiles.

B. Lightly Damaged Materials

The main effect of carrier diffusion on temperature profiles consists of:

- (i) Higher laser powers are required to raise the surface temperature of a good-quality material than of a damaged material;
- (ii) Temperature profiles in good quality materials are generally wider than in damaged materials;
- (iii) The time (t_m) at which the surface temperature reaches maximum is longer in good quality materials than in damaged materials;

(v) The effect of carrier diffusion on temperature profiles is much stronger for Nd:YAG laser than for ruby laser irradiation.

(vi) The effect of the "sinking" of the carriers is to produce thermal spikes at the surface and lower temperature in the material interior. For a sufficiently fast surface recombination, the profiles may develop a secondary local maximum in the material interior.

The conclusions (i) - (v) are the direct consequence of the model used for the transfer of the photon energy to heat. The excess portion of the electron energy is transferred during the "quasi-thermalization" of the photoexcited carriers, into the volume bounded by α^{-1} . The corresponding heated volume is σ_{eff}

$$\sigma_{\text{eff}} = \max(\alpha^{-1}, (\kappa t_p / c_p)^{1/2}) \quad , \quad (21)$$

and the associated rise in the surface temperature is on the order of

$$\Delta T_{\text{max}}(x=0, t=t_p) \approx \frac{F_0 t_p}{c_p \sigma_{\text{eff}}} \left(1 - \frac{E_g}{h\nu} \right) \quad . \quad (22)$$

The bandgap portion of the energy heats a volume bounded by the depth

$$l_{\text{eff},g} = \max(\sigma_{\text{eff}}, L) \quad , \quad (23)$$

where $L, L = \sqrt{D\tau}$, is the carrier diffusion length. The associated temperature rise is roughly

$$\Delta T_{\text{max}}(x=0, t=t_p) \approx \frac{F_0 t_p}{c_p l_{\text{eff},g}} \frac{E_g}{h\nu} \quad . \quad (24)$$

Thus, in good quality materials where $L > \sigma_{eff}$, the bandgap energy heats a volume which is larger than the one heated by the excess energy. This results in temperatures which are generally lower (for the same laser power) than those in damaged materials. Furthermore, since both the electron lifetime (τ) and the thermal diffusion time associated with the bandgap portion of the energy

$$t_{th,g} = c_p \ell_{eff,g}^2 / 4\kappa \quad , \quad (25)$$

may be quite long; the heating times (t_m and $t_{1/2}$) may be substantially longer than t_p . Clearly, the effect of carrier diffusion on the temperature will be greater for Nd:YAG than for ruby laser irradiation. This is because Nd:YAG frequency is very close to the silicon bandgap frequency; the excess portion of the electron energy is $\approx 1\%$. For ruby irradiation of silicon, the excess portion of the electron energy is large, $\approx 35\%$, and is not affected by electron diffusion.¹⁰

The conclusion (vi) is the unique consequence of the surface recombination of the carriers. For $v_s = 0$, the temperature is smooth and monotonically decreasing with the distance away from the surface. This is because the thermal sources S_1 (optical absorption) and S_2 (carrier distribution) are also monotonically decreasing, and the surface recombination source $S_3 = 0$. For $v_s \neq 0$, however, the carriers preferentially recombine, and release their energy, at the surface. This leads to the formation of thermal spikes. Furthermore, since the carrier distribution develops a "sink" at the surface, the source $S_2(x)$ will be nonmonotonic. If the maximum S_2 is sufficiently strong so that also the total $S = S_1 + S_2$ is nonmonotonic, then the resulting thermal distribution may develop a local interior maximum.

(We note that all peaks and maxima will eventually disappear with time because of carrier and/or thermal diffusion.)

Figures 1 and 2 show carrier distributions for silicon, with time (t/t_p) and v_s as parameters. In Figure 1, the electron lifetime is 10^{-9} sec, in Figure 2, $\tau = 10^{-7}$ sec. The effect of v_s is clearly seen. The carrier distribution (per unit photon flux) is high and monotonic for $v_s = 0$, lower and nonmonotonic for $v_s \neq 0$. For short τ (Figure 1), the maximum is sharp and close to the surface. The maximum moves into the material interior with increasing v_s and higher t/t_p . Because of the short τ ($\tau < t_p$), the distribution decays extremely rapidly after the end of the pulse ($t > t_p$). For longer τ ($\tau \geq t_p$, see Figure 2), the maximum is much more pronounced. The concentration remains high even when $t > t_p$.

Inspection of Figures 3-12 reveals the qualitative features discussed above.

Ruby Irradiation of GaAs

Figures 3, 4, and 5 show temperature distributions for ruby laser irradiation of GaAs. Figures 3 and 4 show the effect of v_s . The principal effect of large v_s in GaAs is to lower the surface temperature. For the same laser input, the surface temperature obtained for $v_s = 2 \times 10^4 \text{ cm s}^{-1}$ is higher (by $\approx 50\%$) than the temperature obtained for $v_s = 2 \times 10^7 \text{ cm s}^{-1}$. Figures 4 and 5 compare temperature distributions for heavily damaged and good quality GaAs. The principal effect of the electron diffusion is to increase the laser power required for heating good quality material in Figure 5, approximately by $(1 - E_g/h\nu)^{-1} \approx 5$ (for the same α). Its effect

on the width of the profiles is negligible; the widths of profiles shown in Figures 4 and 5 are practically identical. This is because in good quality material, the bandgap energy (80% of the photon energy) is distributed into the depth $L \approx 3 \times 10^{-3}$ cm, which is much larger (by nearly two orders of magnitude) than the depth for the excess energy (20%), $\alpha^{-1} \approx 5 \times 10^{-5}$ cm. This makes the bandgap portion of the energy ineffective for the heating. We should note that for intermediately damaged GaAs, more of the available power will be used for the heating, and for $\alpha^{-1} \approx L$, the profiles will be somewhat wider than in either the heavily damaged or high quality materials.

Ruby Irradiation of Silicon

Figures 6 - 7 show, respectively, temperature distributions in lightly damaged and good quality silicon irradiated by ruby laser radiation. We have also simulated profiles in amorphous silicon. The power requirements and shapes of these profiles were very much the same as those shown for GaAs. This was because of the similar input parameters ($\alpha = 2 \times 10^4 \text{ cm}^{-1}$, $\tau \leq 10^{-9}$ sec) used in these calculations.

Figure 6 corresponds to a lightly damaged crystalline silicon ($\alpha = 2 \times 10^3 \text{ cm}^{-1}$). The main differences between amorphous and crystalline silicon are higher power requirements and longer heating times for crystalline materials. The higher powers are required because of (i) weaker optical absorption, and (ii) inefficient utilization of the bandgap portion of the energy for the heating in good quality materials. The heating times ($t_{1/2} \approx 100 t_p$ in Figure 6) are long because of the influence of the bandgap energy on temperature (for $\tau > t_p$) at long

times (in Figure 6, $\tau = 10 t_p$). At short times, the profile width is $\approx \alpha^{-1}$, as only the excess energy heats the material at $t < \tau$.

Figure 7 corresponds to a good quality material ($\tau = 10^{-5}$ sec, $D = 30 \text{ cm}^2 \text{ s}^{-1}$). The interesting feature to notice in Figure 7 is that at times $t \approx 100 t_p$, the profile width is narrower than the one shown in Figure 6. This is because at long τ and D the bandgap energy has practically no effect on the heating (at sufficiently short times). For $L > \alpha^{-1}$, both ΔT_{max} and the halfwidth are governed by the excess portion of the electron energy, the bandgap portion affects the profile only at very long times, $t \gtrsim \tau$.

Nd:YAG Irradiation of Silicon

Several representative profiles are shown in Figures 8-12. For Nd:YAG in silicon, $E_g \approx .99 \text{ eV}$ and the profiles are therefore bandgap recombination dominated. Figures 8 and 9 compare profiles for two values of v_s for heavily damaged material ($\alpha = 10^3 \text{ cm}^{-1}$, $\tau = 10^{-9} \text{ sec}$); $v_s = 2 \times 10^7 \text{ cm s}^{-1}$ and $2 \times 10^4 \text{ cm s}^{-1}$ in Figures 8 and 9, respectively. The halfwidths are $\approx \alpha^{-1} > L$ in both cases. The primary effect of slow v_s ($v_s \tau < L$) in Figure 9 is to slightly increase ΔT_{max} and suppress the interior maximum appearing in Figure 8 for large v_s . There should be a sharp peak at the surface in Figure 8. The peak is unresolved because of the numerical limitations. The peak corresponds to thermal spikes (discussed earlier), created at $x = 0$ as the result of the preferential deposition of the carrier energy at the surface. Several remarks about the effect of $v_s \neq 0$ on the profiles are in order here.

As has already been discussed, the occurrence of thermal spikes and interior maxima (the local maximum is always lower than the spike)

is the consequence of fast surface recombination. By inspecting the simulated profiles, a nonmonotonic $T(x)$ occurs for: v_s sufficiently large, $v_s \tau > L$ (so that maximum in $n(x,t)$ is large and separated from the surface), τ not too short (so that the energy does not relax instantaneously), α^{-1} not too small, $\alpha^{-1} \gtrsim L$ (so that the bandgap energy is not dissipated into too large a volume), and the excess portion of the energy not too large compared to the bandgap energy (so that the source term $S_1(x)$ does not suppress the peak in $S_2(x)$). If these conditions are satisfied, $T(x)$ becomes nonmonotonic, with a sharp spike at the surface and a local maximum at the distance $0 < x < L$ away from the surface. We note that as the carriers diffuse deeper into the material, the local maximum may also move deeper into the interior; it eventually disappears (because of both decreased carrier concentration and thermal diffusion), with the characteristic time $t = \max(\tau, t_p, (c_p/4\kappa)L^2)$. The magnitude of the spike at $x = 0$ can be estimated by using the energy conservation arguments. For example, the energy released by the carriers recombined at the surface must be equal to the heat contained in the spike. We then obtain that in the limit of rapid v_s , short τ , and large α , the height of the spike is on the order of $\Delta T_{\text{peak}} \approx \alpha T_0 \sqrt{v_s \ell_s / \kappa c_p}$, where ℓ_s is the characteristic length associated with the position of the maximum in $\Delta n(x,t)$. For typical parameters of interest, this yields $\Delta T_{\text{peak}} \approx \text{several } 10^3 \text{ K}$ and spike characteristic width $\ell_p \approx \sqrt{\ell_s \kappa / c_p v_s} \approx 10^{-6} \text{ cm}$.

Figure 10 corresponds to light-to-intermediately damaged material ($\alpha \approx 10^3 \text{ cm}^{-1}$, $\tau \approx 10^{-7} \text{ sec}$). The development of nonmonotonic $\Delta T(x,t)$ is clearly seen (again, there should be a spike at $x = 0$). The temperature becomes monotonic at times $t \gtrsim t_{\text{th,e}} \approx (c_p/4\kappa)L^2 \approx 10^{-6} \text{ sec}$. Because of the long τ , the required

power is about twice higher than the one for the heavily damaged material in Figure 9 (for otherwise the same parameters). Figures 11 and 12 show the effect of the electron diffusivity D on the profiles. The main effect of increasing D (at constant τ , $\tau \sim 10^{-6}$ sec) is to suppress the interior maximum. Because of the long τ , the heating times are very long, the temperature is high even at time $t \gtrsim 100 t_p$.

We have also simulated profiles for $\alpha = 100 \text{ cm}^{-1}$, and 500 cm^{-1} . On the scaled distances αx , the shapes of the profiles were qualitatively similar to those calculated for $\alpha = 10^3 \text{ cm}^{-1}$. The required powers were also much higher (approximately by the ratio of α 's), and the heating times accordingly longer (as determined by the thermal time $(c_p/4\kappa)l_{\text{eff},g}^2$, see Eq. 25).

IV. DISCUSSION

In order to facilitate a more comprehensive understanding of our results, Figures 13 and 14 show the derived dependence of (i) pulse energy (Q) required to raise the surface temperature by $\Delta T \approx 1,400^\circ\text{C}$, (ii) time at which the surface temperature reaches its maximum (t_m), and (iii) time at which the temperature drops to one-half of its maximum value ($t_{1/2}$), on the quality of the processed material (silicon only). The quality is characterized in terms of the electron diffusion length L (the corresponding values of τ and D and α are also indicated). We emphasize once again that the values of the material parameters used are some "average" representative values (this is true particularly for the values of α for Nd:YAG irradiation of silicon) and thus the values of the derived parameters are very approximate. The derived

$Q(Q = F t_p)$ is the actually absorbed energy: the incident energy is nearly twice as high as the absorbed energy, because of material reflection. The laser parameters have the same values as those used in Section III; the results could be generalized to different values.

A. Ruby in Silicon

The required energy increases with L increasing, from about $Q \approx .25\text{J}$ for amorphous, to $Q \approx 4\text{ J}$ for good quality material. Only the excess portion of the energy is operative for heating of the quality material ($E_g/h\nu \approx 65\%$), and, therefore, Q saturates at long L ; this is seen in Figure 13. With the α 's and t_p used, the heated volume is thermal diffusion-dominated for amorphous material and optical absorption depth-limited for good quality material. The surface temperature reaches maximum at $t_m = t_p$. The effect of the bandgap portion of the energy is to slow down the temperature decay in lightly damaged materials. At intermediate values of L , $L \gtrsim \alpha^{-1}$, the temperature remains high up to the time $(c_p/4\kappa)L^2$ (i.e., $t_{1/2} \approx \tau$). At very long L ($L \gg \alpha^{-1}$), however, the bandgap energy is dissipated into an extremely large volume (depth \approx several L), so that its effect on temperature becomes insignificant. The temperature starts to decay more rapidly. The decrease in $t_{1/2}$ is seen in Figure 14 for $L \gtrsim 5 \times 10^{-3}\text{ cm}$.

B. Nd:YAG in Silicon

The heating is nearly entirely bandgap energy-dominated. For amorphous and damaged materials, the optical absorption depth $\alpha^{-1} > (\sigma_{th}, L)$, and the profile width is therefore $\approx \alpha^{-1}$, unaffected by the diffusion. The surface temperature is $\Delta T_{\max} \approx Q\alpha/c_p$. In good quality material, L becomes $\gtrsim 10^{-2}\text{ cm}$.

This is larger than the probable value of α^{-1} in the material, $\alpha^{-1} \approx 2 \times 10^{-3}$ cm for lightly damaged, and $\alpha^{-1} \approx 10^{-2}$ cm for good quality material. Therefore, the depth of the heated volume is $\approx L$, and the power required to heat the material increases accordingly. In Figure 13, Q increases at long L with L approximately linearly.

Because the heating is bandgap energy-dominated, the maximum value of the temperature in good quality materials is obtained at time t_m , generally longer than t_p (for the amorphous and heavily damaged material, $t_m \approx t_p$). For good quality material, t_m is on the order of several τ . The decay of the surface temperature is determined by the thermal diffusion time $t_{th,g}$ ($t_{1/2} = t_{th,g} = \max[(c_p/4\kappa)L^2, (c_p/4\kappa)\frac{1}{\alpha^2}, t_p]$). Since the thickness of the heated region increases with L increasing, there is no saturation of $t_{1/2}$ at long L which has been observed for ruby irradiation of silicon.

In summary, we have investigated in this work the influence of the diffusion of the photoexcited carriers on laser-heating of strongly absorbing semiconductors. The diffusion was found to increase the power required to heat good quality materials, and to prolong the heating times. Surface recombination was found to create thermal spikes at the surface. The temperature profiles calculated in this work indicate that, under certain conditions, the temperature distribution may become nonmonotonic. The nonmonotonic profile is the consequence of the interplay of surface recombination and diffusion of the photoexcited carriers. The position of the interior maximum is dependent upon both the bulk quality and the properties of the surface. The strength of the thermal spike can be estimated from energy arguments.

In practice, the existence of the thermal spikes may be of importance for annealing of localized defects. For a sufficiently strong spike, it is qualitatively feasible for the heat to dissolve the defect. This

results in localized defect removal. For practical utilization, further analyses are desirable. This is because of the effect of both the finite size (e.g., finite thickness of the surface "dead layer"), and spatial distribution, of the defects on the temperature profiles. Further effects, not considered here, include other energy "diffusion" mechanisms (such as radiative recombination of the carriers), non-equilibrium effects, and distributed damage such as that created during ion implantation. The damaged regions have different optical, thermal, and electronic properties than the rest of the material (they often absorb the radiation more strongly). Furthermore, as the damage disappears, material properties change during the processing. This was not taken into account here; in the model used, with the exception of the front surface, the material was assumed homogeneous, and its properties independent of time. Further analyses are being planned to account for these effects.

ACKNOWLEDGEMENTS

The author wishes to thank Drs. R. S. Witte, S. Prussin, W. von der Ohe and L. Heflinger for technical discussions concerning the laser annealing; Drs. P. Molmud and T. J. Wilcox for mathematical discussions, and R. Lipkis for her help in computer calculations.

APPENDIX A: ELECTRON TRANSPORT EQUATION: SOLUTION BY LAPLACE TRANSFORM TECHNIQUE

A.1. Problem

The diffusion equation we want to solve is

$$\frac{\partial n}{\partial t} = \alpha F(t) e^{-\alpha x} - \frac{(n - n_0)}{\tau} + D \frac{\partial^2 n}{\partial x^2}, \quad (\text{A.1})$$

We consider constant α , τ and D , and a square-shape generation function $F(t)$:

$$F(t) = \begin{cases} F_0 & 0 < t < t_p \\ 0 & \text{otherwise.} \end{cases} \quad (\text{A.2})$$

The boundary conditions are:

Front surface:

$$D \frac{\partial n}{\partial x} \bigg|_{x=0} = v_s (n(0,t) - n_0) \quad (\text{A.3})$$

Back surface:

$$n(x = \ell) = n_0 \quad (\text{A.4})$$

The initial condition is

$$n(x, t=0) = n_0 \quad (\text{A.5})$$

Equation (A.1) is a linear partial differential equation for $n(x,t)$. For $v_s = 0$, Eq. (A.1) can be solved by using the Green's function technique. For $v_s \neq 0$, it is solved by using the Laplace transform technique. In using the Laplace transforms, advantage is taken of the knowledge of the steady state solution to (A.1).

A.2. Case $v_s = 0$: Green's Function Technique

For $v_s = 0$, Green's function is

$$G(x, x', t - t') = \frac{1}{\sqrt{4\pi D(t - t')}} \sum_{n=-\infty}^{+\infty} (-1)^n e^{-t/\tau} \left\{ \exp\left(-\frac{(x-x' - 2n\ell)^2}{4D(t - t')}\right) + \exp\left(-\frac{(x+x' - 2n\ell)^2}{4D(t - t')}\right) \right\}, \quad (\text{A.6})$$

and $\Delta n \equiv n(x, t) - n_0$ is

$$\Delta n(x, t) = \int_0^\infty dx' \int_0^{t_p} G(x, x', t - t') \alpha F_0 \exp[-\alpha x] \quad (\text{A.7})$$

Assuming the slab thickness $\ell \gg \alpha^{-1}$, the semiconductor can be replaced by a semi-infinite medium, with the result that the summation \sum_n in Eq. (A.6) reduces to only one term, namely the term $n=0$. Substituting the resulting Equation into Eq. (A.7) and integrating it over coordinate x yields:

$$\Delta n(x, t) = \frac{\alpha F_0}{2} \sum_{(\pm)} \exp[\pm \alpha x] \int_{t_0}^t dt' \exp\left[-\frac{t'}{\tau}(1 - \alpha^2 L^2)\right] \text{erf c}\left(\frac{\pm x + 2\alpha D t'}{2\sqrt{D t'}}\right), \quad (\text{A.8})$$

where $L = \sqrt{D\tau}$, $\text{erf c}(z)$ is the complementary error function, and the integral lower boundary t_0 is

$$t_0 = \begin{cases} 0 & t < t_p \\ t - t_p & t > t_p \end{cases} \quad (\text{A.9})$$

Integral (A.8) is evaluated by using the partial fraction. This yields

$$\Delta n(x,t) = \frac{\alpha \tau F_0}{2(\alpha^2 L^2 - 1)} \sum_{(+,-)} \exp(\pm \alpha x) \left\{ \exp\left[\frac{-t'}{\tau} (1 - \alpha^2 L^2)\right] \operatorname{erfc}\left[\frac{\pm x + 2\alpha D t'}{2\sqrt{D t'}}\right] \right\}_{t_0}^t$$

$$+ \frac{2}{\sqrt{\pi}} \int_{t_0}^t dt' \exp\left[\frac{-t'}{\tau} (1 - \alpha^2 L^2)\right] \exp(\pm \alpha x) \left(\pm \frac{x}{4\sqrt{D}} t'^{3/2} + \frac{\alpha\sqrt{D}}{2\sqrt{t'}} \right) \exp\left[-\left(\frac{x^2}{4D t'} + \alpha^2 D t'\right)\right] \Bigg\} \quad (\text{A.10})$$

The second term on the right hand side of Eq. (A.10) is evaluated by using the following change of variables,

$$t = z^{-2}, \quad \text{and} \quad t' = z'^2 \quad (\text{A.11})$$

for the first and second term under the integral sign, respectively. Performing the change of the variables, each of the two terms transforms into an expression of the type ($a \neq 0$)

$$\int \exp\left(-a^2 z'^2 - \frac{b^2}{z'^2}\right) dz' = \frac{\sqrt{\pi}}{4a} \sum_{(+,-)} \exp(\pm 2ab) \operatorname{erf}\left(az' \pm \frac{b}{z'}\right) + \text{constant} . \quad (\text{A.12})$$

Collecting the resulting terms completes the calculation. The final result is

$$\Delta n(x,t) = \frac{\alpha \tau F_0}{2(\alpha^2 L^2 - 1)} \left\{ \exp\left[-(1 - L^2 \alpha^2) \frac{t}{\tau}\right] \sum_{(+,-)} e^{\pm \alpha x} \operatorname{erfc}\left(\alpha \sqrt{D t} \pm \frac{x}{\sqrt{4D t}}\right) \right.$$

$$\left. + \alpha L \sum_{(+,-)} e^{\pm \frac{x}{L}} \operatorname{erf}\left(\sqrt{\frac{t'}{\tau}} \pm \frac{x}{\sqrt{4D t'}}\right) \right\}_{t_0}^t \quad (\text{A.13})$$

A.3. Case $v_s \neq 0$: Laplace Transform Technique

Since the steady-state solution to Eq. (A.1) is known, Eq. (A.1) is Laplace-transformed with respect to time. One obtains (for the square-shaped $F(t)$):

$$\frac{\alpha F_0}{s} e^{-\alpha x} (1 - e^{-st_p}) - (s + \frac{1}{\tau}) \Delta \bar{n}(x, s) + D \frac{\partial^2 \bar{n}(s, x)}{\partial x^2} = 0, \quad (\text{A.14})$$

where $\bar{n} = \bar{n}(s, t)$ is the Laplace transform of $n(x, t)$. The solution of (A.13) is

$$\Delta \bar{n}(x, s) = \frac{\alpha F_0 \tau}{s} \frac{(1 - e^{-st_p})}{(1 + s\tau - \alpha^2 L^2)} \left\{ e^{-\alpha x} - \frac{v_s + \alpha D}{v_s + \sqrt{D(\frac{1}{\tau} + s)}} \exp\left(-\frac{x}{L} \sqrt{1 + s\tau}\right) \right\}. \quad (\text{A.15})$$

The reverse Laplace transform is easiest to find by using the well-known results for the partial expressions appearing in Eq. (A.15), and making time convolutions of the partial Laplace transforms. That is,

$$F(t) = \int_0^t F_1(t - t') F_2(t') dt' \quad , \quad (\text{A.16})$$

where

$$\bar{f}_1(s) \rightarrow F_1(t)$$

$$\bar{f}_2(s) \rightarrow F_2(t)$$

$$\bar{f}_1(s) \bar{f}_2(s) \rightarrow F(t)$$

$$\bar{f}(s + c) \rightarrow F(t) e^{-ct}$$

$$\bar{f}(as) \rightarrow \frac{1}{a} F\left(\frac{t}{a}\right)$$

The partial transforms used in evaluating the inverse Laplace transform of Eq. (A.15) are of the type

$$\frac{e^{-as}}{s(s+b)} \rightarrow \begin{cases} \frac{1}{b}(1 - e^{-b(t-a)}) H(t-a) & a > 0 \\ \frac{1}{b}(1 - e^{-bt}) & a \leq 0 \end{cases} \quad (\text{A.17})$$

and

$$\frac{e^{-a\sqrt{s}}}{b + \sqrt{s}} \rightarrow \frac{1}{\sqrt{\pi t}} \exp\left(-\frac{a^2}{4t}\right) - b \exp(ab + b^2 t) \operatorname{erfc}\left(\frac{a}{2\sqrt{t}} + b\sqrt{t}\right). \quad (\text{A.18})$$

In Eq. (A.17), $H(t)$ is the step function. $H(t) = 1$ for $t > 0$ and zero otherwise.

Using (A.16) - (A.18), the inverse transform of Eq. (A.15) is

$$\begin{aligned} \Delta n(x, t) = & \frac{\alpha \tau F_0}{1 - \alpha^2 L^2} \left[e^{-\alpha x} \left\{ 1 - \exp\left[-\frac{t'}{\tau}(1 - L^2 \alpha^2)\right] \right\} \right]_{t_0}^t \\ & - \frac{(v_s + \alpha D)}{D} \int_0^t e^{\frac{t'}{\tau}} \left\{ \sqrt{\frac{D}{\pi t'}} e^{-\frac{x^2}{4Dt'}} - v_s \exp\left[\frac{v_s}{D}(x + v_s t')\right] \operatorname{erfc}\left(\frac{x}{\sqrt{4Dt'}} + v_s \sqrt{\frac{t'}{D}}\right) \right\} \\ & \times \left\{ 1 - \exp\left[-\frac{t-t'}{\tau}(1 - \alpha^2 L^2)\right] - \left(1 - \exp\left[-\frac{(t-t'-t_p)}{\tau}(1 - \alpha^2 L^2)\right]\right) H(t-t'-t_p) \right\} dt' \quad (\text{A.19}) \end{aligned}$$

Integral (A.19) is evaluated by using the same changes of variables as those used for evaluation of integrals in the Green's function expression in Appendix A.2 (viz., Eq. (A.8) and the following discussion). It is convenient to rewrite Eq. (A.19) in the form:

$$\Delta n(x,t) = \frac{\alpha \tau F_0}{1-\alpha^2 L^2} \left\{ e^{-\alpha x} \exp \left[-\frac{t'}{\tau} (1-\alpha^2 L^2) \right]_{t_0}^t - \frac{(v_s + \alpha D)}{D} \right. \\ \left. \times \int_0^t f(t') \left(1-g(t') \exp \left[\frac{t}{\tau} (1-\alpha^2 L^2) \right] - \left(1-g(t') \exp \left[-\frac{(t-t_p)}{\tau} (1-\alpha^2 L^2) \right] \right) H(t-t'-t_p) \right) dt' \right\}, \quad (A.20)$$

where

$$f(t) = e^{-\frac{t}{\tau}} \left\{ \frac{e^{-\frac{x^2}{4Dt}}}{\sqrt{\frac{\pi t}{D}}} - v_s \exp \left[\frac{v_s}{D} (x+v_s t) \right] \operatorname{erfc} \left[\frac{x}{2\sqrt{Dt}} + v_s \sqrt{\frac{t}{D}} \right] \right\}, \quad (A.21)$$

$$g(t) = \exp \left[\frac{t}{\tau} (1-\alpha^2 L^2) \right]. \quad (A.22)$$

The solution of Eq. (A.20) is

$$\Delta n(x,t) = \frac{\alpha \tau F_0}{1-\alpha^2 L^2} \left\{ -\exp \left[-\alpha x - \frac{t'}{\tau} (1-\alpha^2 L^2) \right] - \frac{v_s + \alpha D}{D} \right. \\ \left. \times \left(F(t') - (G(t') - G(0)) \exp \left[\frac{t'}{\tau} (1-\alpha^2 L^2) \right] \right) \right\}_{t_0}^t \quad (A.23)$$

where

$$F(t) = \int dt' f(t') + \text{constant} \quad (A.24)$$

$$G(t) = \int dt' f(t') g(t') + \text{constant} \quad (A.25)$$

The first term in the integral on the right-hand side of Eq. (A.24) is evaluated by using the change of the variables $t' = z^2$. The resulting integral is of the type of Eq. (A.12). The second term under the integration sign is evaluated by first using the partial fraction, and then making the change of the variables, $t' = z^{-2}$ in the two resulting integral expressions. The integral is of the type

$$\int dt e^{-a^2 t - \frac{b^2}{t}} \left(-\frac{\beta}{t^{3/2}} + \frac{\alpha}{\sqrt{t}} \right) = \frac{\sqrt{\pi}}{2} \sum_{(+,-)} e^{\pm 2ab} \left(\frac{\alpha}{a} \pm \frac{\beta}{b} \right) \operatorname{erf} \left(a\sqrt{t} \pm \frac{b}{\sqrt{t}} \right). \quad (\text{A.26})$$

Integral (A.25) is evaluated by using the same procedure. In fact, the only difference between the integrals, Eq. (A.24) and Eq. (A.25), is the replacement of τ^{-1} in Eq. (A.24) by $\alpha^2 D$ in Eq. (A.25).

$$f(t, \tau) g(t, \tau) \rightarrow f(t, \frac{1}{D\alpha^2}). \quad (\text{A.27})$$

The mathematics is then straightforward, though rather tedious. After having collected and combined all terms, the final result is

$$\begin{aligned} \Delta n(x, t) = & \frac{\alpha F_0 \tau}{2(1 - L^2 \alpha^2)} \left\{ \sum_{(+,-)} \left(\frac{1 + \alpha D/v_s}{\pm 1 - \frac{L}{v_s \tau}} \right) e^{\pm \frac{x}{L}} \operatorname{erf} \left(\pm \frac{x}{\sqrt{4Dt'}} + \sqrt{\frac{t'}{\tau}} \right) \right. \\ & + \sum_{(+,-)} \frac{(\pm 1 + D\alpha/v_s)}{(1 - D\alpha/v_s)} \exp \left[\pm \alpha x - \frac{t'}{\tau} (1 - \alpha^2 L^2) \right] \operatorname{erfc} \left(\pm \frac{x}{\sqrt{4Dt'}} + \alpha \sqrt{Dt'} \right) \\ & + \frac{2(1 - L^2 \alpha^2)}{(\alpha D/v_s - 1)(1 - v_s^2 \tau/D)} \exp \left[\frac{-t'}{\tau} + (t' v_s + x) \frac{v_s}{D} \right] \operatorname{erfc} \left(v_s \sqrt{\frac{t'}{D}} + \frac{x}{\sqrt{4Dt'}} \right) \Bigg\}^t_{\max(0, t-t_p)} \end{aligned} \quad (\text{A.28})$$

It is easy to verify that Eq. (A.28) reduces to Eq. (A.13) in the limit of $v_s = 0$. In the steady state, Eq. (A.28) reduces to the well-known expression,

$$\lim_{t_p, t \rightarrow \infty} \Delta n(x, \infty) = \frac{\alpha \tau F_0}{1 - \alpha^2 L^2} \left\{ e^{-\alpha x} - \frac{v_s + \alpha D}{v_s + \frac{L}{\tau}} e^{-x/L} \right\}. \quad (\text{A.29})$$

REFERENCES

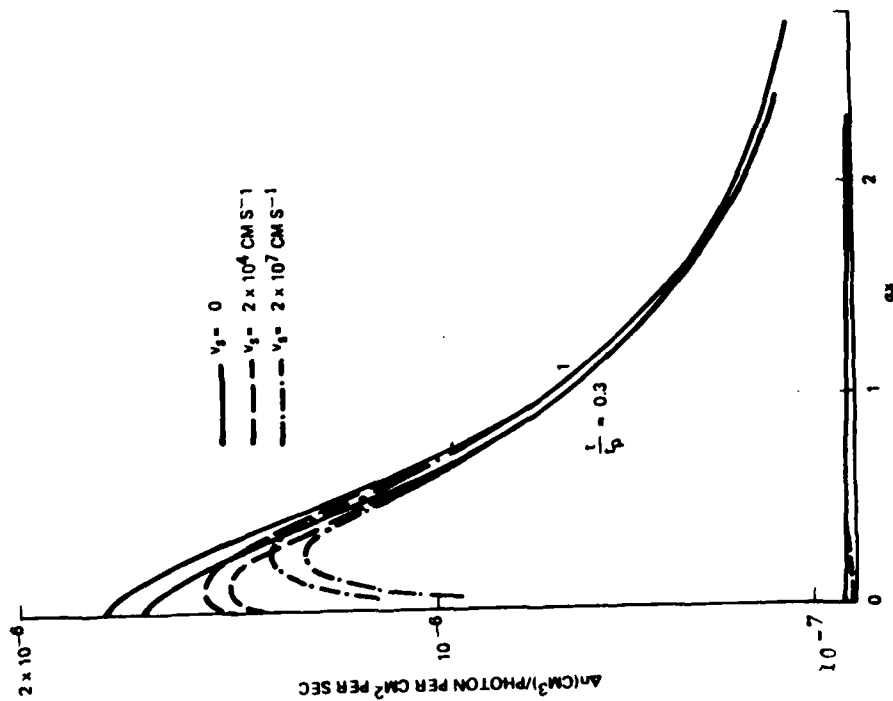
1. For a review article, see C. W. White, J. Narayan, and R. T. Young, "Laser Annealing of Ion-Implanted Semiconductors," *Science*, Vol. 204, 401 (4 May 1979).
2. See, for example, R. T. Young, C. W. White, G. J. Clark, J. Navayan, W. H. Christie, M. Murakami, P. W. King, and S. D. Kramer, "Laser Annealing of Boron-Implanted Silicon, *Appl. Phys. Letters*, 32 (3), 139 (1978), and references in (1).
3. P. Baeri, S. U. Campisano, G. Foti, and E. Rimini, "Arsenic Diffusion in Silicon Melted by High Power Nanosecond Laser Pulsing," *Appl. Phys. Letters*, 33 (2), 137 (1978); D. H. Austen, C. M. Surko, T.N.C. Venkatesan, R. E. Slusher, and J. A. Golovchenko, "Time Resolved Reflectivity of Ion-Implanted Silicon During Laser Annealing," *Appl. Phys. Letters*, 33 (5), 437 (1978); J. C. Schultz, and R. J. Collins, "A Computer Simulation of Laser Annealing Silicon at 1.06 μm ," *Appl. Phys. Letters*, 34 (1), 84 (1979), and references in (1).
4. See, for example, A. Gat, J. F. Gibbons, I. J. Magee, J. Peng, V. Deline, P. Williams, C. A. Evans, Jr., "Physical and Electrical Properties of Laser-Annealed Ion-Implanted Silicon," *Appl. Phys. Letters*, 32, 276 (1978); T.N.C. Venkatesan, J. A. Golovchenko, J. M. Poate, P. Cowan, and G. K. Celler, "Dose Dependence in the Laser Annealing of Arsenic-Implanted Silicon," *Appl. Phys. Letters*, 33 (5), 429 (1978); G. K. Celler, J. M. Poate and L. C. Kimerling, "Spatially Controlled Crystal Regrowth of Ion-Implanted Silicon by Laser Irradiation," *Appl. Phys. Letters*, 32 (8), 464 (1978), and references in (1).

5. S. A. Prussin, W. von der Ohe, and R. S. Witte, "Annealing of Low Fluence Implanted Silicon," presented at 21st Electronic Materials Conference (EMC), University of Colorado at Boulder, June 27-29, 1979.
6. Other mechanisms include photon-phonon interaction and free absorption. We have made estimates of the free carrier absorption and found that for laser intensities of interest the effect is small at the ruby laser wavelength. However, it may become large at the Nd:YAG laser wavelength. The photon-phonon and free electron absorptions were not taken into account in this work.
7. The pulse lengths (t_p) are on the order of 10^{-8} - 10^{-7} seconds. The thermal diffusion time (time it takes the thermal energy to diffuse a distance α^{-1} away from the semiconductor surface) is $t_{th} \approx c_p / \kappa \alpha^2 \approx 10^{-8}$ to 10^{-6} sec for $\alpha = 10^4 \text{ cm}^{-1}$ to 10^3 cm^{-1} , respectively. The time it takes the electron (provided that electron lifetime is long enough that the electron does not recombine earlier, $L > \alpha^{-1}$), to traverse distance α^{-1} is $t_e = 1/D\alpha^2 \approx 10^{-9}$ seconds for the typical value of $D \approx 10 \text{ cm}^2 \text{ s}^{-1}$.
8. S. M. Sze, Physics of Semiconductor Devices, Wiley-Interscience, New York (1969).
9. It is well known that, for Nd:YAG irradiation α increases rapidly with temperature. For single crystal silicon, $\alpha \approx 10 \text{ cm}^{-1}$ at 300°K and increases by approximately two orders of magnitude at the melting temperature. This was not taken into account; the values used are some representative average values.
10. Equations (21) - (25) assume that the thermal diffusions associated with the two heat sources are independent of each other. In reality, of course, this is not the case. The equations provide a convenient, though an approximate, means for quantifying the general features of the derived results.

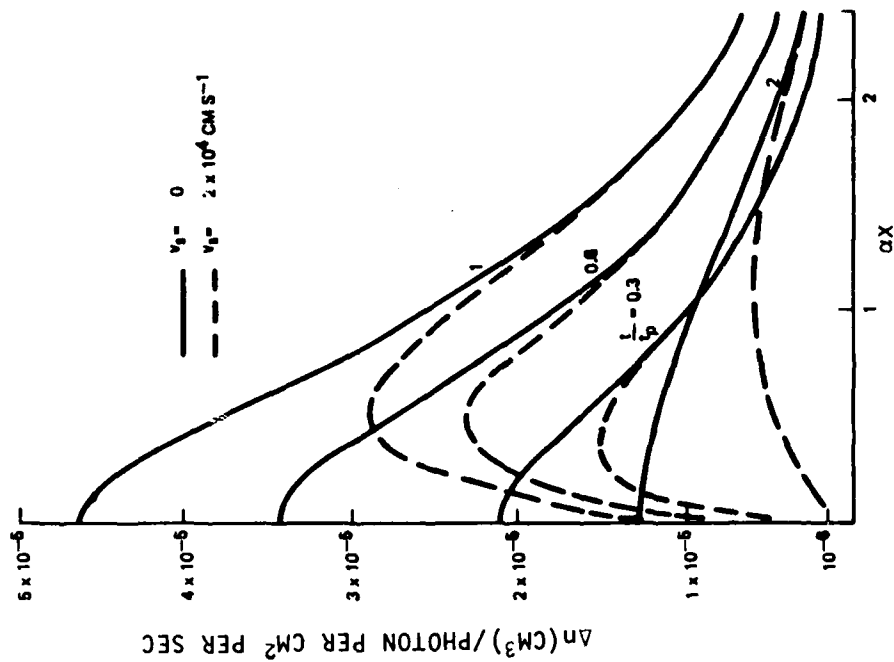
LIST OF FIGURES

1. Photocarrier concentration in ruby-irradiated silicon, $t_p = 10^{-8}$ sec, $\alpha = 2 \times 10^3 \text{ cm}^{-1}$, $\tau = 10^{-9}$ sec, $D = 3 \text{ cm}^2 \text{ s}^{-1}$. For $v_s \neq 0$, $n(x,t)$ is nonmonotonic. Since $\tau \ll t_p$, $n(x,t)$ decays rapidly after $t > t_p$.
2. Photocarrier concentration in Nd:YAG-irradiated silicon, $t_p = 10^{-7}$ sec, $\alpha = 10^3 \text{ cm}^{-1}$, $\tau = 10^{-7}$ sec, $D = 3 \text{ cm}^2 \text{ s}^{-1}$. For $v_s \neq 0$, $n(x,t)$ is nonmonotonic. Since $\tau \approx t_p$, $n(x,t)$ is still high at $t = t_p$.
3. Temperature for ruby irradiation of heavily damaged GaAs: $\tau = 10^{-11}$ sec, $D = 15 \text{ cm}^2 \text{ s}^{-1}$, $v_s = 2 \times 10^7 \text{ cm s}^{-1}$, $\alpha = 2 \times 10^4 \text{ cm}^{-1}$, $t_p = 10^{-8}$ sec, $F_0 = 2 \times 10^7 \text{ W/cm}^2$.
4. Temperature for ruby irradiation of heavily damaged GaAs: $\tau = 10^{-11}$ sec, $D = 15 \text{ cm}^2 \text{ s}^{-1}$, $v_s = 2 \times 10^4 \text{ cm s}^{-1}$, $\alpha = 2 \times 10^4 \text{ cm}^{-1}$, $t_p = 10^{-8}$ sec, $F_0 = 2 \times 10^7 \text{ W/cm}^2$.
5. Temperature for ruby irradiation of GaAs: $\tau = 10^{-8}$ sec, $D = 200 \text{ cm}^2 \text{ s}^{-1}$, $v_s = 2 \times 10^4 \text{ cm s}^{-1}$, $\alpha = 2 \times 10^4 \text{ cm}^{-1}$, $t_p = 10^{-8}$ sec, $F_0 = 8 \times 10^7 \text{ W/cm}^2$.
6. Temperature for ruby irradiation of silicon: $\tau = 10^{-7}$ sec, $D = 3 \text{ cm}^2 \text{ s}^{-1}$, $v_s = 2 \times 10^7 \text{ cm s}^{-1}$, $\alpha = 2 \times 10^3 \text{ cm}^{-1}$, $t_p = 10^{-8}$ sec, $F_0 = 2.5 \times 10^8 \text{ W/cm}^2$.
7. Temperature for ruby irradiation of good quality silicon: $\tau = 10^{-5}$ sec, $D = 30 \text{ cm}^2 \text{ s}^{-1}$, $v_s = 2 \times 10^4 \text{ cm s}^{-1}$, $\alpha = 2 \times 10^3 \text{ cm}^{-1}$, $t_p = 10^{-8}$ sec, $F_0 = 4 \times 10^8 \text{ W/cm}^2$.
8. Temperature for Nd:YAG irradiation of damaged silicon: $\tau = 10^{-9}$ sec, $D = 3 \text{ cm}^2 \text{ s}^{-1}$, $v_s = 2 \times 10^7 \text{ cm s}^{-1}$, $\alpha = 10^3 \text{ cm}^{-1}$, $t_p = 10^{-7}$ sec, $F_0 = 2.5 \times 10^7 \text{ W/cm}^2$.
9. Temperature for Nd:YAG irradiation of damaged silicon: $\tau = 10^{-9}$ sec, $D = 3 \text{ cm}^2 \text{ s}^{-1}$, $v_s = 2 \times 10^4 \text{ cm s}^{-1}$, $\alpha = 10^3 \text{ cm}^{-1}$; $t_p = 10^{-7}$ sec, $F_0 = 2.5 \times 10^7 \text{ W/cm}^2$.
10. Temperature for Nd:YAG irradiation of silicon: $\tau = 10^{-7}$ sec, $D = 3 \text{ cm}^2 \text{ s}^{-1}$, $v_s = 2 \times 10^4 \text{ cm s}^{-1}$, $\alpha = 10^3 \text{ cm}^{-1}$, $t_p = 10^{-7}$ sec, $F_0 = 7 \times 10^7 \text{ W/cm}^2$.

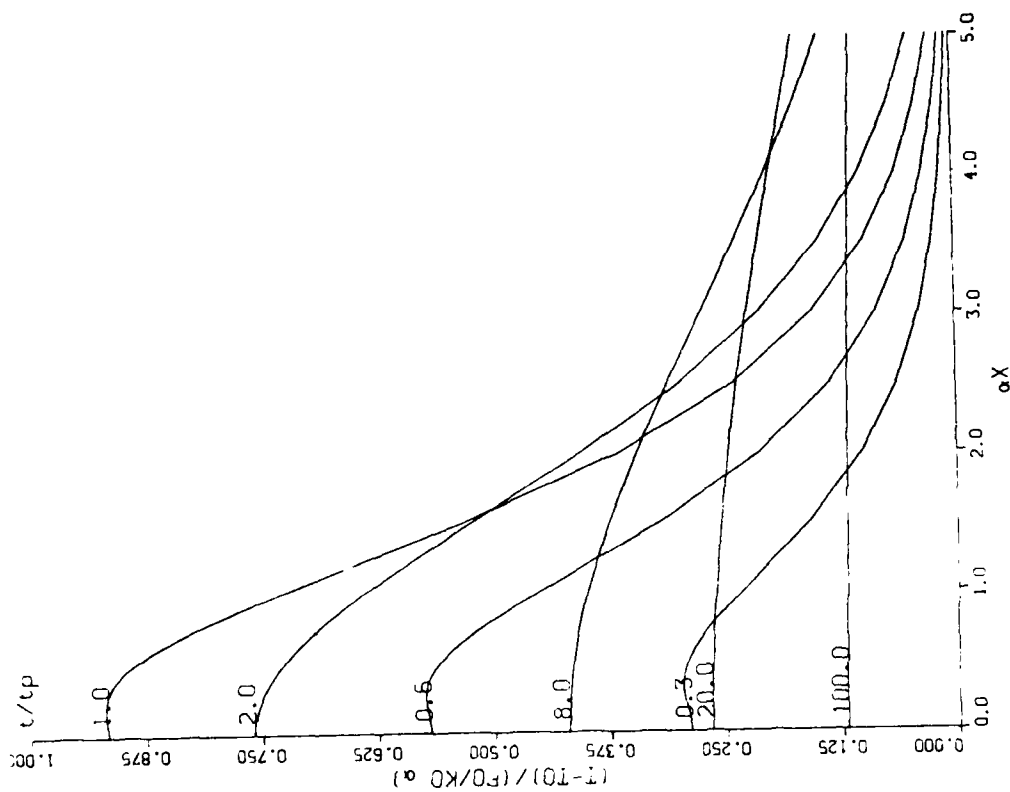
11. Temperature for Nd:YAG irradiation of silicon. $\tau = 10^{-6}$ sec,
 $D = 3 \text{ cm}^2 \text{ s}^{-1}$, $v_s = 2 \times 10^4 \text{ cm s}^{-1}$, $\alpha = 10^3 \text{ cm}^{-1}$, $t_p = 10^{-7}$ sec,
 $F_0 = 2 \times 10^8 \text{ W/cm}^2$.
12. Temperature for Nd:YAG irradiation of silicon. $\tau = 10^{-6}$ sec,
 $D = 30 \text{ cm}^2 \text{ s}^{-1}$, $v_s = 2 \times 10^4 \text{ cm s}^{-1}$, $\alpha = 10^3 \text{ cm}^{-1}$, $t_p = 10^{-7}$ sec,
 $F_0 = 2.5 \times 10^8 \text{ W/cm}^2$.
13. Laser energy (Q) required to heat the silicon surface just below
the melting temperature. Nd:YAG: $t_p = 10^{-7}$ sec; ruby: $t_p = 10^{-8}$ sec.
14. The dependence of (i) time at which the surface temperature reaches
the maximum (t_m); time when the surface temperature decays to 1/2
of its maximum value ($t_{1/2}$), on material quality (silicon).



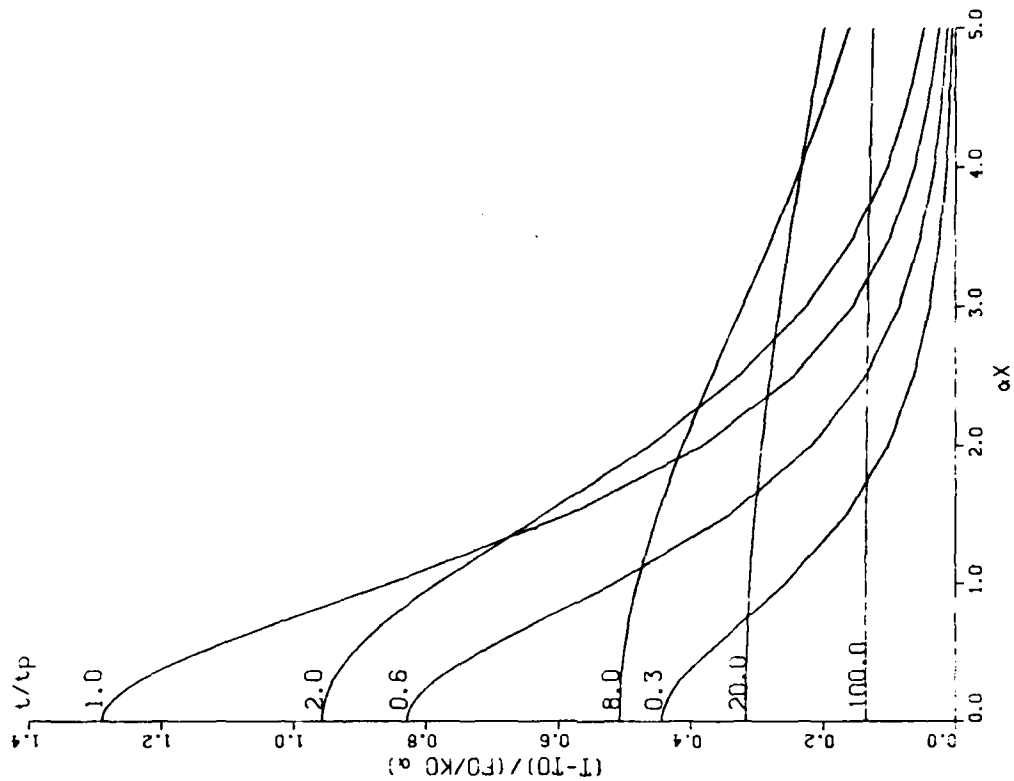
1. Photocarrier concentration in ruby-irradiated silicon, $t_p = 10^{-8}$ sec, $\alpha = 2 \times 10^3 \text{ cm}^{-1}$, $\tau = 10^{-9}$ sec, $D = 3 \text{ cm}^2 \text{ s}^{-1}$. For $v_s \neq 0$, $n(x, t)$ is nonmonotonic. Since $\tau \ll t_p$, $n(x, t)$ decays rapidly after $t > t_p$.



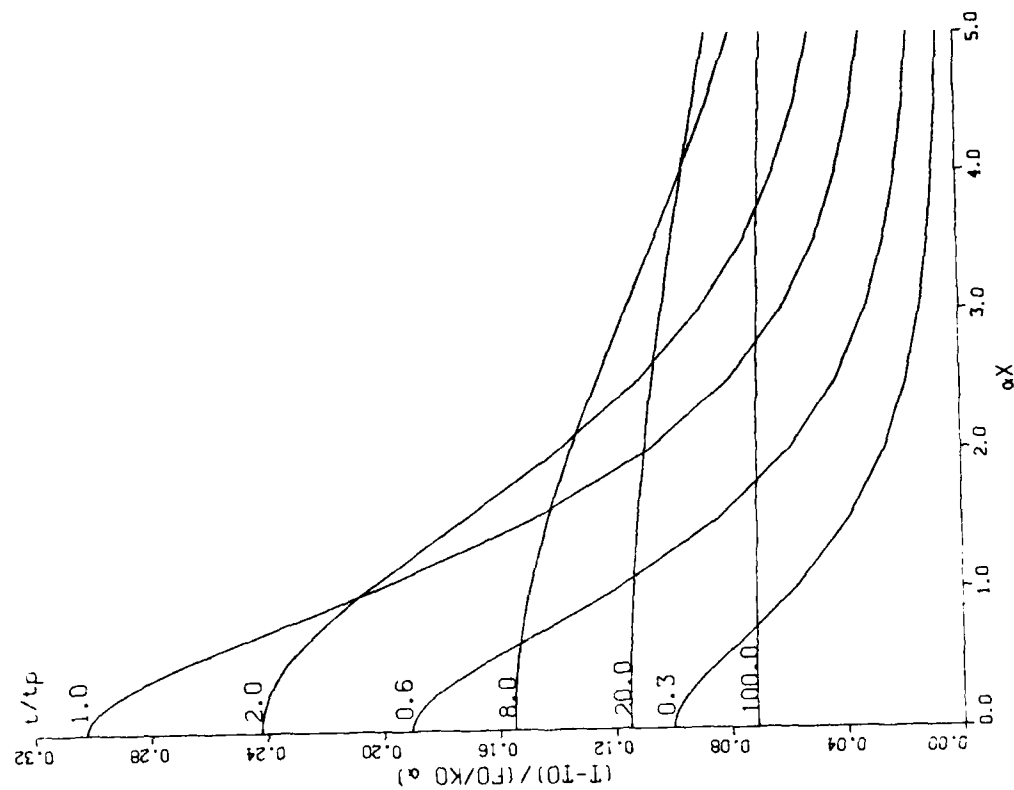
2. Photocarrier concentration in Nd:YAG-irradiated silicon, $t_p = 10^{-7}$ sec, $\alpha = 10^3 \text{ cm}^{-1}$, $\tau = 10^{-7}$ sec, $D = 3 \text{ cm}^2 \text{ s}^{-1}$. For $v_s \neq 0$, $n(x, t)$ is nonmonotonic. Since $\tau \approx t_p$, $n(x, t)$ is still high at $t = t_p$.



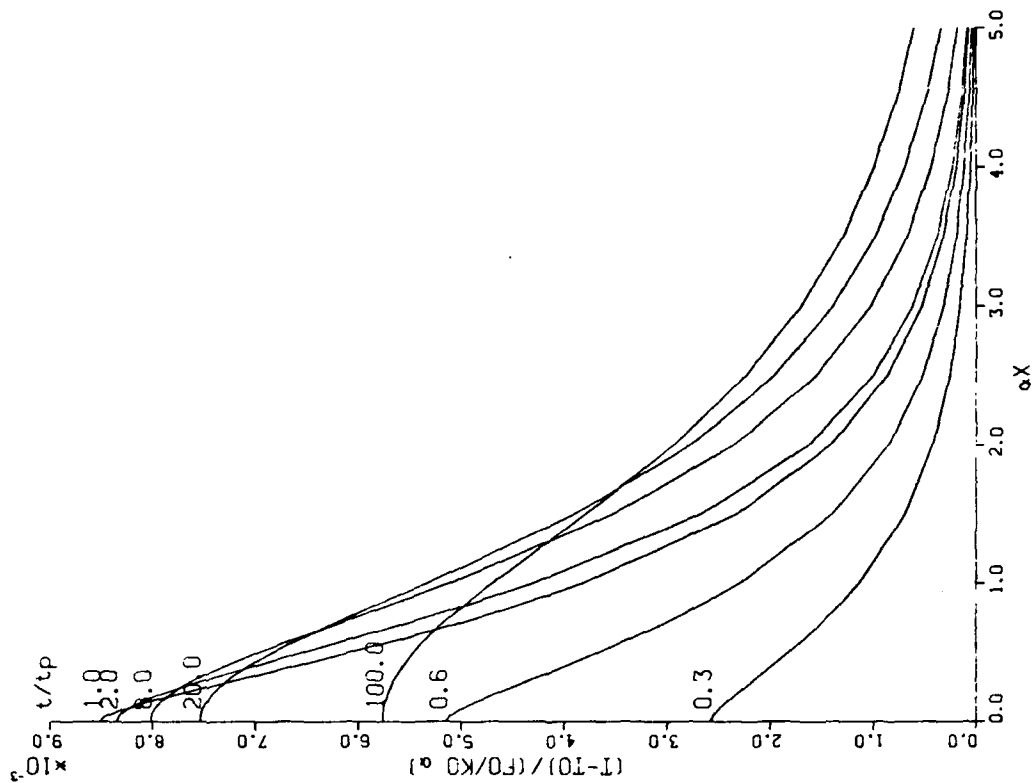
3. Temperature for ruby irradiation of heavily damaged GaAs: $\tau = 10^{-11}$ sec,
 $D = 15 \text{ cm}^2 \text{ s}^{-1}$, $\nu_s = 2 \times 10^7 \text{ cm s}^{-1}$, $\alpha = 2 \times 10^4 \text{ cm}^{-1}$, $t_p = 10^{-8}$ sec,
 $F_0 = 2 \times 10^7 \text{ W/cm}^2$.



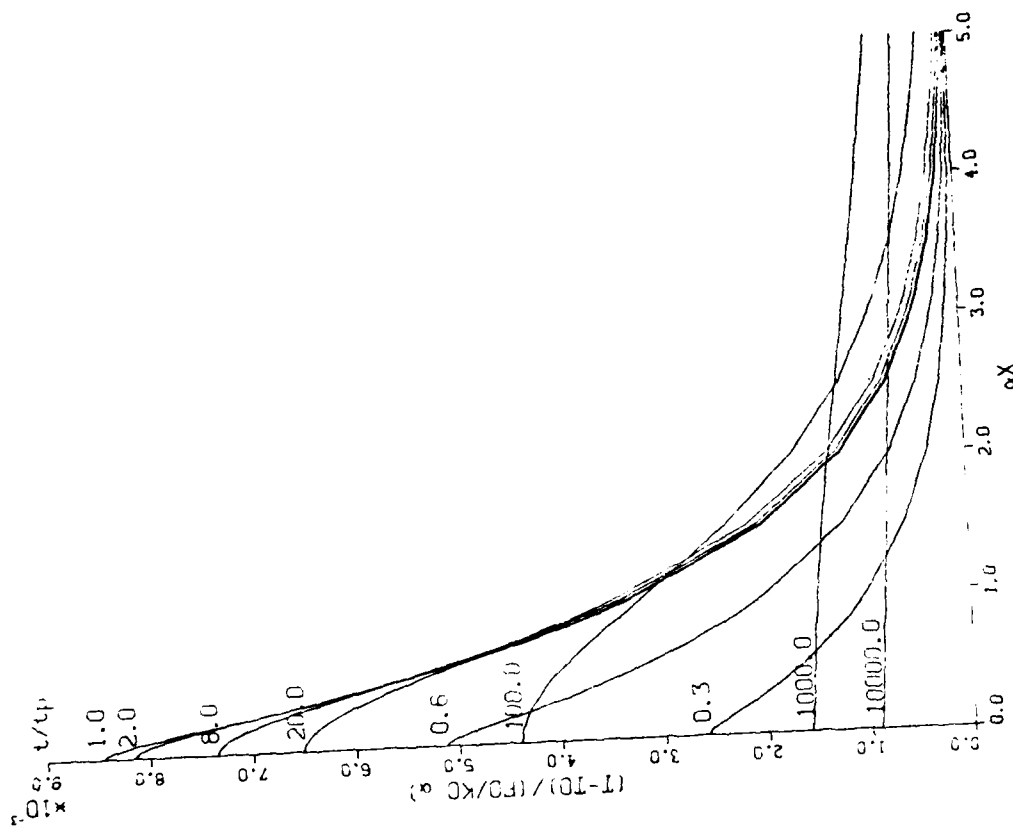
4. Temperature for ruby irradiation of heavily damaged GaAs: $\tau = 10^{-11}$ sec,
 $D = 15 \text{ cm}^2 \text{ s}^{-1}$, $\nu_s = 2 \times 10^6 \text{ cm s}^{-1}$, $\alpha = 2 \times 10^4 \text{ cm}^{-1}$, $t_p = 10^{-8}$ sec,
 $F_0 = 2 \times 10^7 \text{ W/cm}^2$.



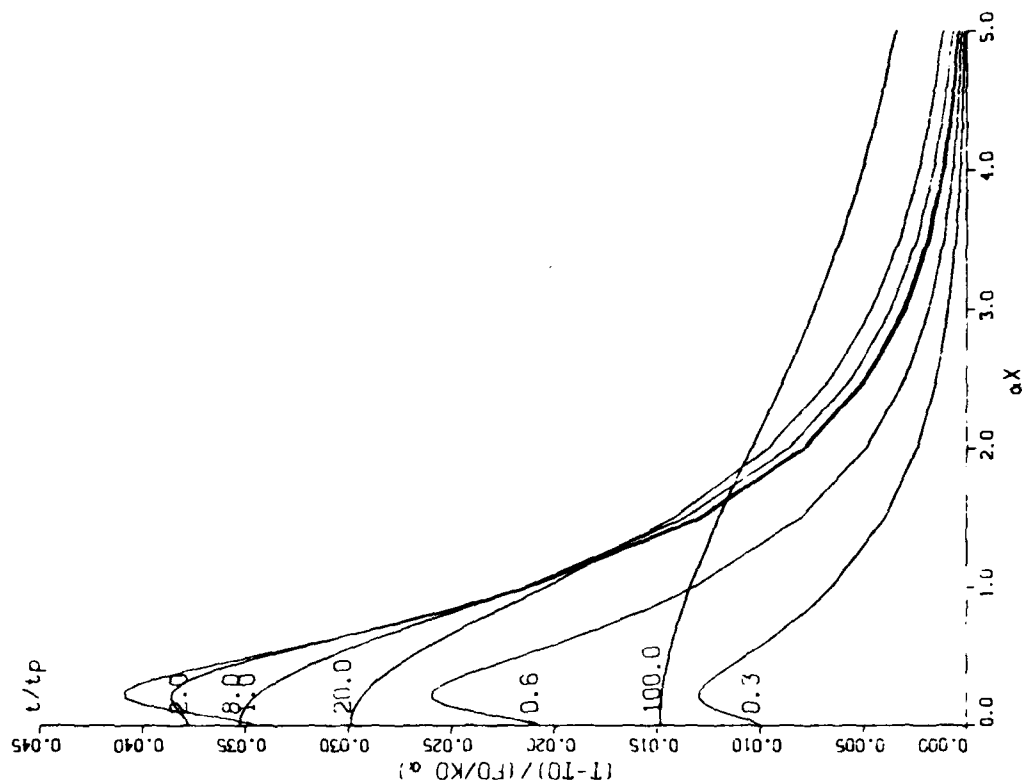
5. Temperature for ruby irradiation of GaAs: $\tau = 10^{-8}$ sec, $D = 200 \text{ cm}^2 \text{ s}^{-1}$, $v_s = 2 \times 10^4 \text{ cm s}^{-1}$, $\alpha = 2 \times 10^4 \text{ cm}^{-1}$, $t_p = 10^{-8}$ sec, $F_0 = 8 \times 10^7 \text{ W/cm}^2$.



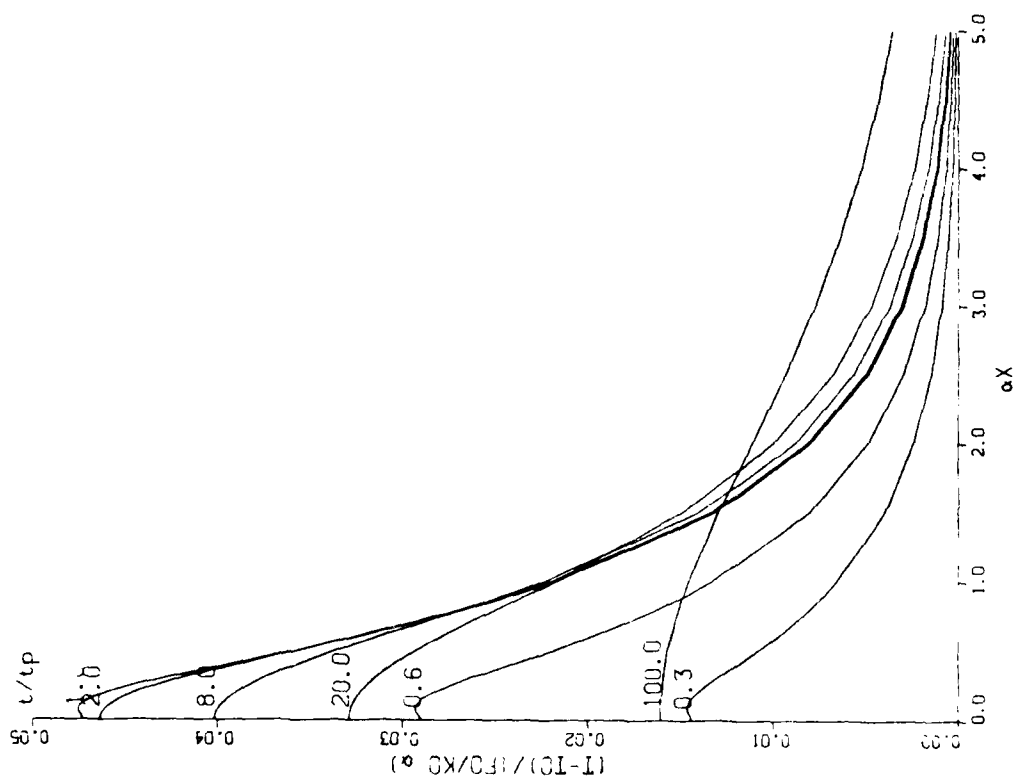
6. Temperature for ruby irradiation of silicon: $\tau = 10^{-7}$ sec, $D = 3 \text{ cm}^2 \text{ s}^{-1}$, $v_s = 2 \times 10^7 \text{ cm s}^{-1}$, $\alpha = 2 \times 10^3 \text{ cm}^{-1}$, $t_p = 10^{-8}$ sec, $F_0 = 2.5 \times 10^8 \text{ W/cm}^2$.



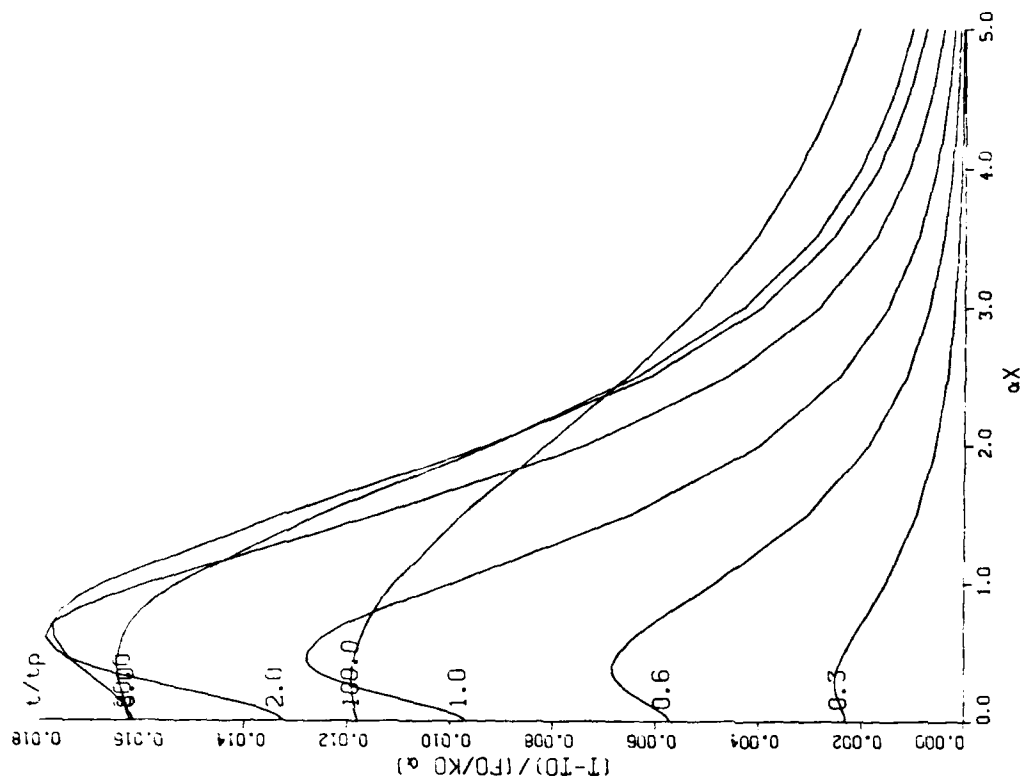
7. Temperature for ruby irradiation of good quality silicon:
 $\tau = 10^{-5}$ sec, $D = 30 \text{ cm}^2 \text{ s}^{-1}$, $V_s = 2 \times 10^4 \text{ cm s}^{-1}$, $\alpha = 2 \times 10^3 \text{ cm}^{-1}$,
 $t_p = 10^{-8}$ sec, $F_0 = 4 \times 10^8 \text{ W/cm}^2$.



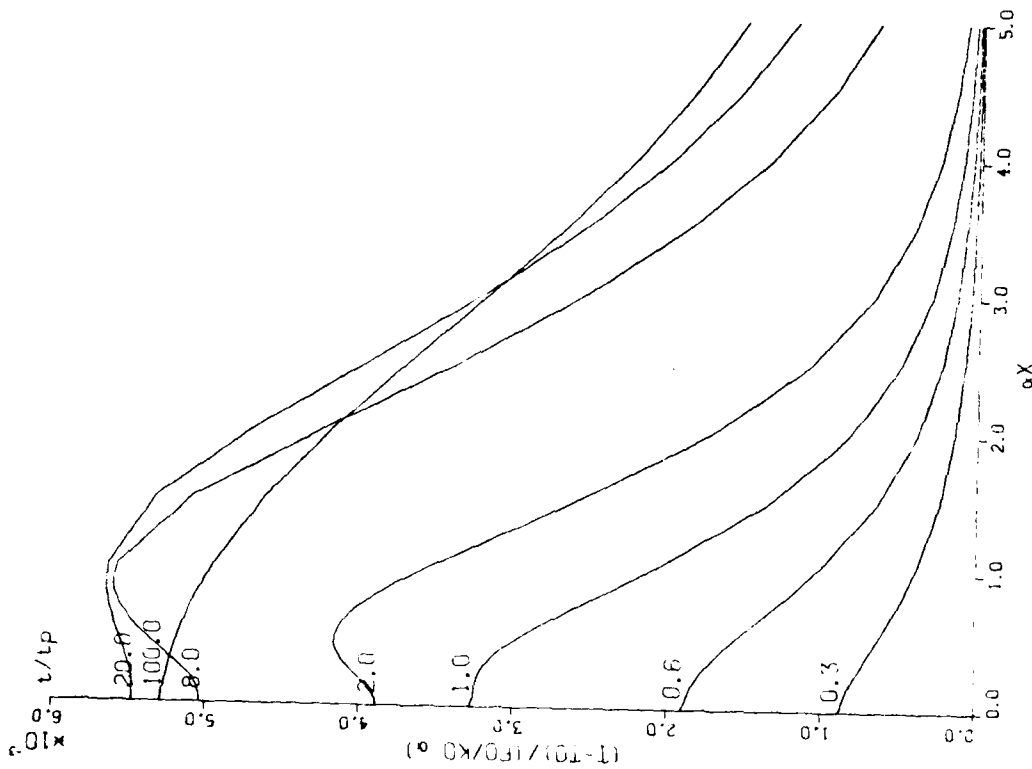
8. Temperature for Nd:YAG irradiation of damaged silicon: $\tau = 10^{-9}$ sec,
 $D = 3 \text{ cm}^2 \text{ s}^{-1}$, $V_s = 2 \times 10^7 \text{ cm s}^{-1}$, $\alpha = 10^3 \text{ cm}^{-1}$, $t_p = 10^{-7}$ sec,
 $F_0 = 2.5 \times 10^7 \text{ W/cm}^2$.



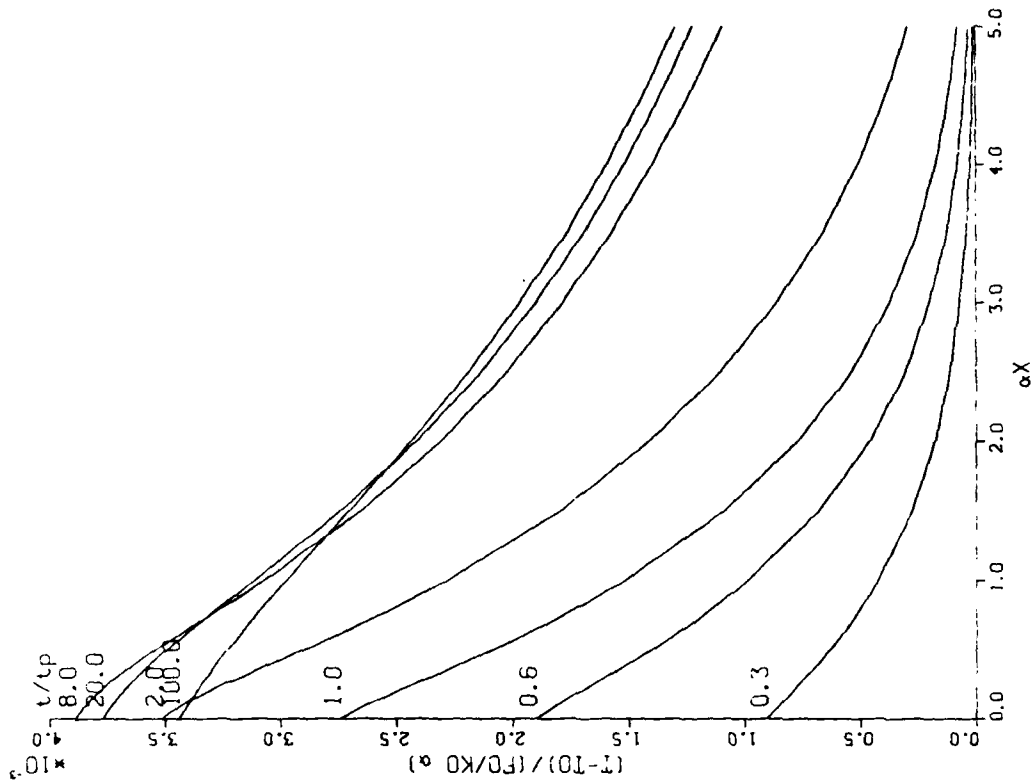
9. Temperature for Nd: YAG irradiation of damaged silicon: $\tau = 10^{-9}$ sec,
 $D = 3 \text{ cm}^2 \text{ s}^{-1}$, $v_s = 2 \times 10^4 \text{ cm s}^{-1}$, $\alpha = 10^3 \text{ cm}^{-1}$; $t_p = 10^{-7}$ sec,
 $F_0 = 2.5 \times 10^7 \text{ W/cm}^2$.



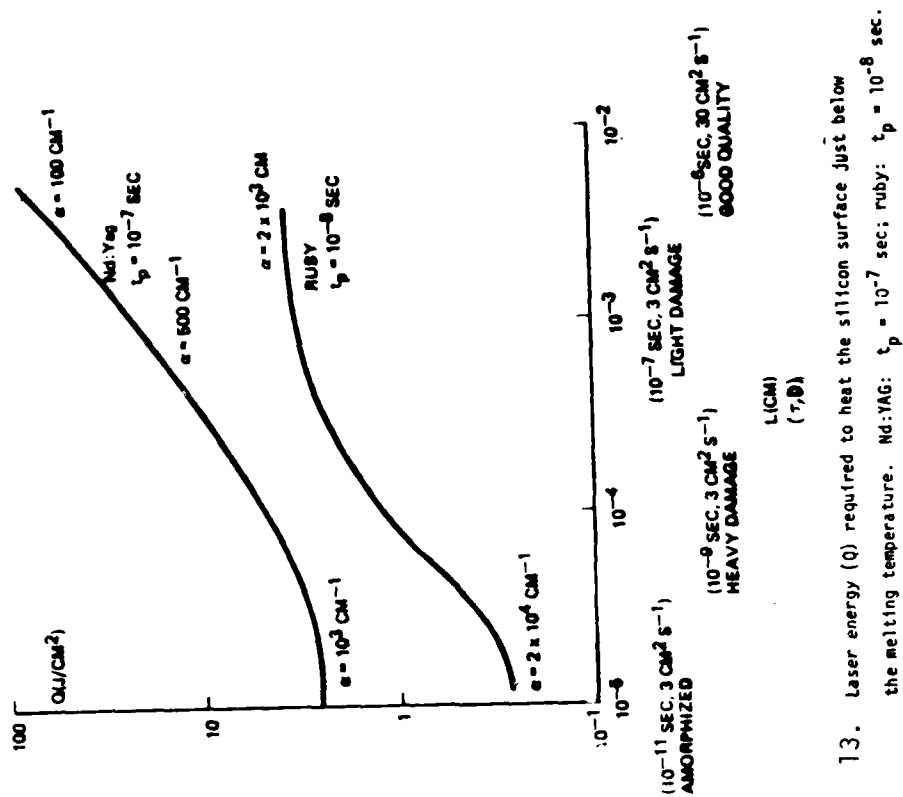
10. Temperature for Nd: YAG irradiation of silicon: $\tau = 10^{-7}$ sec,
 $D = 3 \text{ cm}^2 \text{ s}^{-1}$, $v_s = 2 \times 10^4 \text{ cm s}^{-1}$, $\alpha = 10^3 \text{ cm}^{-1}$, $t_p = 10^{-7}$ sec,
 $F_0 = 7 \times 10^7 \text{ W/cm}^2$.



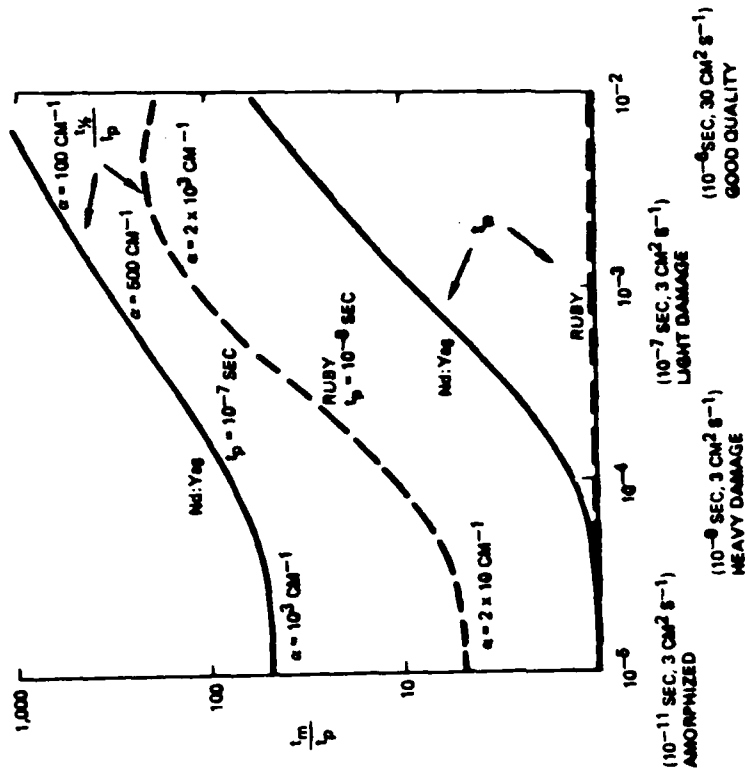
17. Temperature for Nd:YAG irradiation of silicon. $\tau = 10^{-6}$ sec,
 $D = 3 \text{ cm}^2 \text{ s}^{-1}$, $\nu_s = 2 \times 10^4 \text{ cm s}^{-1}$, $\alpha = 10^3 \text{ cm}^{-1}$, $t_p = 10^{-7}$ sec,
 $F_0 = 2 \times 10^8 \text{ W/cm}^2$.



12. Temperature for Nd:YAG irradiation of silicon. $\tau = 10^{-6}$ sec,
 $D = 30 \text{ cm}^2 \text{ s}^{-1}$, $\nu_s = 2 \times 10^4 \text{ cm s}^{-1}$, $\alpha = 10^3 \text{ cm}^{-1}$, $t_p = 10^{-7}$ sec,
 $F_0 = 2.5 \times 10^8 \text{ W/cm}^2$.



13. Laser energy (Q) required to heat the silicon surface just below the melting temperature. Nd:YAG: $t_p = 10^{-7}$ sec; Ruby: $t_p = 10^{-8}$ sec.



14. The dependence of (t) time at which the surface temperature reaches the maximum (t_m); time when the surface temperature decays to 1/2 of its maximum value ($t_{1/2}$), on material quality (silicon).

APPENDIX B

LASER ANNEALING OF LOW FLUENCE
ION IMPLANTED SILICON

S. Prussin

TRW Semiconductors

Lawndale , CA 90260

and

W. von der Ohe

TRW Defense and Space Systems Group

One Space Park, Redondo Beach, CA 90278

ABSTRACT

Laser Annealing of Low Fluence Ion Implanted Silicon

S. Prussin, TRW Semiconductors, 14520 Aviation Blvd.,
Lawndale, CA 90260 and W. von der Ohe, TRW Defense
and Space Systems Group, One Space Park, Redondo Beach,
CA 90278.

Ruby laser pulses of 1.5 to 2.5 J cm⁻² were shown to be effective in dissolving defect nuclei in {100} and {111} silicon surfaces implanted with 10¹⁴ to 10¹⁵ B cm⁻² and 10¹⁴ to 5 x 10¹⁴ P cm⁻². No melting and only partial electrical activation occurred. A sequential moderate thermal anneal, 10 min at 1000°C, results in full electrical activation without significant impurity redistribution. A {111} silicon surface, made amorphous by an ion implantation of 5 x 10¹⁴ P cm⁻² was electrically activated and completely cleared of defect nuclei without melting by preceding the laser anneal by a two step thermal anneal (30 min at 550°C, 10 min at 1000°C). The mechanism of pulse laser annealing of non-amorphous ion implanted surfaces is discussed.

LASER ANNEALING OF LOW FLUENCE
ION IMPLANTED SILICON

1. INTRODUCTION

Ion implantation has been found to result in the introduction of electrically active impurities in an extremely uniform and reproducible manner. Concomitant with this desirable characteristic, ion implantation leaves a residue of lattice defects. These primary defects consist of impurity atoms on non-lattice positions, and the presence of many silicon vacancies and interstitials. A relatively moderate thermal anneal, 1000°C for 10 minutes, results in relocation of the impurity atoms to lattice positions as shown by their electrical activation. There is however a considerable residuum of lattice damage remaining. These secondary defects ⁽¹⁾ have been studied by TEM for both light and heavy implantations and have been shown to consist primarily of dislocation loops, with and without enclosed stacking faults. ⁽²⁾ For heavy implantations the Rutherford ion-backscattering and ion-channel technique has been used to show the presence of residual defects. ⁽³⁾ A method developed by the author ⁽⁴⁾ utilizes a two step technique. By growing a thermal oxide, extrinsic dislocation loops are found to expand to a size of several microns. Using chemical etching techniques the intersection of these ternary defects with the surface can be

observed by optical or scanning electron microscopy. This method was applied to boron & phosphorus over the range of 10^{13} to 10^{15} cm^{-2} . A thermal anneal of 1 hr at 1100°C in dry N_2 was effective for 10^{14} cm^{-2} but not for 10^{15} cm^{-2} fluences in dissolving the defect nuclei introduced by the ion implantation so that a subsequent oxidation failed to result in the development of expanded dislocation loops. ⁽⁴⁾ This however causes a significant redistribution of the implanted impurities.

In this study a Q-switched ruby laser was used. A review of the literature, as well as a recent review article indicates that this laser has only been effectively used when the implant fluences were high enough to convert the surface to an amorphous condition. ⁽⁵⁾ Under such conditions it was found that the laser beam melts the crystal to a depth somewhat greater than that of the implanted profile. This molten layer recrystallizes from the undamaged substrate generating an epitaxially grown defect-free single crystalline silicon layer containing the implanted impurity atoms in normal lattice sites. ⁽⁵⁾ Thus both defect elimination and electrical activation of the dopant atoms are simultaneously carried out. During the time the implanted region is molten, the impurity atoms diffuse rapidly in the liquid, resulting in a significant redistribution of the implanted dopant atoms.

It has been suggested that the time available for annealing with Q-switched ruby lasers is too short for an unmolten damaged layer to be annealed with a single pulse and that melting followed by liquid phase epitaxy is essential for effective annealing.⁽⁵⁾

Continuous Ar laser annealing was applied by A. Gat et al.⁽⁶⁾ to silicon surfaces implanted with fluences of As heavy enough, $5 \times 10^{14} \text{ cm}^{-2}$ at 100 keV, to convert the surface to an amorphous condition. Melting did not occur and thus also no redistribution of the implanted As. Fewer defects remained than were found for a single step thermal anneal (30 min at 1000°C) but complete elimination of defect nuclei did not occur.

In this study we chose B implant fluences of 10^{14} , 5×10^{14} and 10^{15} cm^{-2} and P implant fluences of 10^{14} and $5 \times 10^{14} \text{ cm}^{-2}$ into both {100} and {111} silicon surfaces. One implantation, that of $5 \times 10^{14} \text{ P cm}^{-2}$ into a {111} surface, resulted in amorphism. For the rest of the wafers, the surfaces retained their single crystallinity.

For these lower fluence implants it was found that laser energies which were described in the literature as resulting in melting of the surface and completely activating the implanted impurity atoms here failed to heat the silicon surfaces sufficiently to permit more than a fraction of the

implanted dopant atoms to migrate to substitutional positions. Nevertheless the temperature distribution within the implanted layer was such that complete solution of implant defect nuclei occurred. By combining a laser anneal with a short thermal anneal it was possible to achieve both defect elimination as well as complete electrical activation. Such a process would avoid impurity redistribution, permitting the dopant distribution to remain as implanted.

II. EXPERIMENTAL INVESTIGATION

Twenty wafers were subjected to implantation with boron and phosphorus ions. The orientations, conductivity types and resistivities of the wafers, together with the fluences and implant energies are given in Table I. The implant energies were chosen to give similar distributions for the B and P ions. The wafers were commercially polished and had resistivities in the range of 1-4 Ωcm . After implantation the wafers were examined for the presence of amorphism. This was determined by the presence of a characteristic "milky" appearance of the implanted area as compared to the adjacent areas protected from implantation by the wafer holder.⁽²⁾ Wafers 216A and 216B exhibited such amorphism.

After implantation the series A wafers were subjected to an identical laser annealing process and the series B

wafers were halved, each half being subjected to a separate laser annealing process. Figure 1 describes the experimental procedure.

The laser annealing was carried out with a Q-switched ruby laser operated in the multimode condition. The pulse duration was 15 nsecs and the beam size was approximately 1 cm in diameter. The beam was projected through a rectangular aperture 4.4 mm by 7.9 mm. For the A wafers, large areas, approximately one fourth of the surface of each 2 inch diameter wafer, were pulsed with a single laser energy. This was accomplished by using pulses of the same energy, as the wafer was repeatedly translated a distance equal to the width or height of the projected beam. Figure 2 illustrates the laser pulse distribution. The laser energies utilized were 1.0, 1.5, 2.0 and 2.5 J cm⁻². After laser annealing, all surfaces were examined by high power optical microscopy. The rippled appearance characteristic of surface melting ⁽⁷⁾ was not found. In the center of each wafer there remained a small reference area which was not subjected to laser annealing. The laser annealed areas were sufficiently large to permit a sheet resistance value to be obtained directly without introducing correction factors.

Tables II and III list the results of the sheet resistance measurements following the laser annealing. A minimum

of 6 readings was taken for each annealed area and the average taken. For the two lower energies there was considerable scatter while for the higher two energies all readings were within $\pm 5\%$ of the mean. This would appear possibly to be due to inhomogeneities within the laser beam. For the higher energies, lateral thermal conduction could smooth out the annealing effect.

After measuring the sheet resistances of the laser annealed areas all wafers were subjected to a thermal anneal of 10 minutes at 1000°C in an N_2 atmosphere. The results of sheet resistance measurements repeated on the same laser annealed areas are found in Table IV.

As seen in Fig. 1, the B series wafers were halved, one half designated as B1 and the other as B2. The B1 halves were subjected to laser annealing at 9 discrete areas. Each area was $4.4 \text{ mm} \times 7.9 \text{ mm}$, the size of the aperture through which the beam was projected. The laser energies used were $.5, 1.0, 1.5, 2.0$ and 2.5 J cm^{-2} with a single pulse as well as $.5 (2\text{X}), .5 (4\text{X}), 1.0 (2\text{X}),$ and $1.0 \text{ J cm}^{-2} (3\text{X})$. Each discrete laser annealed area was surrounded by a non annealed area and after oxidation and Sirtl etching, the laser pulse boundary (LPB) was examined by optical microscopy and compared to the ion implant boundary (IIB) between the area of the wafer covered by the wafer holder and the area of the wafer subjected

to implantation without laser annealing. The results are listed in Table V.

Wafers 116B and 216B received identical implantations of $5 \times 10^{14} \text{ Pcm}^{-2}$, but only 216B with a {111} orientation exhibited amorphism. The wafer halves 116B2 and 216B2 were subjected to a pre-anneal treatment of 1 h at 550°C to permit slow transformation of the amorphous layer to single crystallinity. This was confirmed by the disappearance of the "milky" surface on 216B2. All B2 halves were then annealed for 10 min at 1000°C . Sheet resistivity measurements were carried out and are given in Table IV under the heading of zero laser beam energy.

The B2 halves were then subjected to laser annealing at 5 discrete areas, using single laser pulsed of .5, 1.0, 1.5, 2.0 and 2.5 J cm^{-2} . Each discrete laser annealed area, $4.4 \text{ mm} \times 7.9 \text{ mm}$, was surrounded by a non annealed area. After steam oxidation and Sirtl etching, the surfaces were examined by optical microscopy. The results are listed in Table VI.

III. EXPERIMENTAL RESULTS

Examination of the results listed in Tables II and III shows that in every case there is a significant increase in electrical activity of the implanted ions in going from 1.0 to 1.5 J cm^{-2} and from 1.5 to 2.0 J cm^{-2} . In going from 2.0 to 2.5 J cm^{-2} , the change in R_{\square} appears to be much smaller.

At first it might appear that this is a result of an approach to complete activation. Following the laser anneal with the moderate thermal anneal of 10 minutes at 1000°C results in a very significant decrease in sheet resistance for all specimens for all laser anneals as is shown by comparing Table IV with Tables II and III. This is illustrated in Fig. 3, in which the sheet resistances for laser annealing alone and for combined laser and thermal annealing are compared. We recognize for the fluences studied that laser annealing by itself is incapable of bringing about full electrical activation of the implanted ions.

A measure of the effectiveness of laser pulses in eliminating implant damage is the comparison of the implanted and laser annealed surfaces with that of an unimplanted and unpulsed surface after oxidation and Sirtl etching. Where these are identical we can reasonably assume that the laser annealing eliminated the defect nuclei introduced by the ion implantation. As seen in Table V, this occurred for most of the B1 wafer halves for laser pulses of 1.5 J cm^{-2} and for all of them for 2.0 and 2.5 J cm^{-2} . For a laser pulse of 1.0 J cm^{-2} there was a transitional structure between no annealing and complete annealing. This structure was also found at the LPB of the higher energy laser annealed areas.

Figure 4 illustrates the laser pulse boundary (LPB) for specimen 113B1 for 1.5 J cm^{-2} . The non-pulsed surface is characterized by a light concentration of oxidation stacking faults (OSF), the pulsed area is relatively clear, and the transitional region is characterized by a higher concentration of OSF corresponding to that found for the lower laser energy of 1.0 J cm^{-2} . Figures 5 and 6 illustrate the LPB for specimen 117B1 for 1.5 J cm^{-2} . In Fig. 5 we see the laser annealed area free of OSF on the left and the transition zone containing a heavy concentration of OSF with a light background on the right. In Fig. 6 the transition zone is on the left and the unannealed area containing a heavy background together with a heavy concentration of OSF is found on the right. For a laser energy of 1.0 J cm^{-2} , the annealed area is very similar to the transition area for the 1.5 J cm^{-2} anneal. No results are listed for the lowest laser energy, $.5 \text{ J cm}^{-2}$, since no differences in ternary defect distribution from the non pulsed areas was observed.

In this investigation we also studied the effect of multiple laser pulses of $.5$ and 1.0 J cm^{-2} . From Table V, we note that a laser pulse of 1.0 J cm^{-2} results in a significant reduction of the defect concentration for various implantations while 1.5 J cm^{-2} was effective in eliminating all defects in most cases. It appeared reasonable that multiple pulses of 1.0 J cm^{-2} might be equivalent to a single

pulse of higher energy. It was found however, that multiple pulses of .5 and 1.0 J cm⁻² did not reduce the defect concentration to any significant extent below the level found for a single pulse of the same energy.

Following the thermal anneal of the A series wafers, these too were subjected to steam oxidation and Sirtl etching. Microscopic examination showed results similar to those obtained with the B1 series, confirming our prior experience that an anneal of 1000°C for 10 minutes has little or no effect in dissolving ion implant defect nuclei.

The annealing procedure, 10 min at 1000°C in dry N₂, utilized for the B2 wafer halves prior to laser pulsing converts the ion implant damage into secondary defects.⁽¹⁾ These consist of small dislocation loops, probably resulting from the agglomeration of the primary defects, the vacancies and interstitial atoms generated in the implantation process. The secondary defects appear to be much more stable than the primary defects as shown by their greater resistance to solution by laser annealing. These results are listed in Table VI. For three of the lower fluence specimens, 113B2, 213B2, and 214B2, the expanded implant defect concentration was not sufficiently greater than the background to permit us to detect clearly a LPB. Comparing Table V with Table VI we note that, where in the former a laser energy of 2.0 J cm⁻²

was sufficient to dissolve the defect nuclei in every single specimen, in the latter we find that the higher energy of 2.5 J cm^{-2} results only in partial reduction of the defect concentration with one notable exception, specimen 216B2.

Wafers 216A and B were the only ones of the 20 studied which exhibited amorphism after ion implantation. Specimens 116B2 and 216B2 received identical two step thermal anneals prior to laser pulsing. The first step, 60 min at 550°C , was chosen to permit slow regrowth of the amorphous layer into single crystal silicon. Examination of specimen 216B2 after this step did indeed show that the implanted surface had lost its "milky" appearance and could not be distinguished from the adjacent non-implanted surfaces. Sheet resistivity measurements gave values of $392 \text{ } \Omega/\square$ for 116B2 and $264 \text{ } \Omega/\square$ for 216B2, agreeing with work of Miyao et al⁽⁸⁾ that only partial activation is obtained for 550°C anneals.

The second step, 10 min at 1000°C , was a standard thermal anneal used to produce electrical activation of the implanted impurities. The two step process has been shown to reduce significantly the implant damage for heavier implant fluences⁽⁹⁾.

We found that the use of a two step thermal anneal for this amorphous surface permits us to dissolve the ion implant defect nuclei with a laser pulse energy of 2.0 J cm^{-2} .

This last result suggests that the technique of combined laser and thermal annealing which was developed for low fluence implants as described here might also be effectively applied to heavy implants where the surface is converted to an amorphous condition and therefore prone to melting and concomitant impurity redistribution when subjected to pulsed laser annealing. By introducing a two step thermal anneal, the amorphous surface is solid phase epitaxially regrown without impurity redistribution. Subsequent laser annealing results in the dissolution of the implant defects without melting or the resultant impurity redistribution.

IV. DISCUSSION

The results of this study suggest that the energy release in the interaction of a pulsed ruby laser with a single crystalline surface containing discrete implant defects occurs primarily at the defects, creating localized hot spots which result in the dissolution of the defect and in the heating and electrical activation of the area adjacent to the defect. This phenomenon was clearly illustrated in a separate unpublished study of the interaction of Q switch ruby laser pulses, identical to the ones used in this study, with silicon which had been subjected to neutron bombardment. In that study we found clear signs of the occurrence of localized melting

at the silicon surfaces in the vicinity of defects, Fig. 7. We did not detect such melt spots for ion implanted and laser annealed silicon.

The interaction of a laser pulse with a semiconducting crystal is well understood. For each photon absorbed we generate a hole-electron pair. These have a kinetic energy as well as a potential energy equal to the band gap energy. The kinetic energy is transferred almost immediately to the crystal lattice as heat, while the potential energy is released at such a time and place as recombination of the hole-electron pair occurs.

We recognize that the intensity of a laser pulse, I , in penetrating a distance x from the surface of a homogeneous crystal is given by the relation

$$I = I_0 e^{-\alpha x}$$

where

I_0 is the initial intensity and
 α is the absorptivity.

The concentration of excess hole-electron pairs generated is proportional to the rate of absorption

$$[n] = [p] = -\frac{dI}{dx} = \alpha I(x)$$

The surface volume contains not only the implanted impurities but also a high concentration of crystal defects

which can act as recombination centers for the hole-electron pairs generated by the laser pulse. This permits the generation of high temperatures at defect sites by the diffusion of excess electrons and holes from adjacent areas. A requirement for this model to be applicable is that the rate of diffusion of holes and electrons to the defect recombination centers exceed by a significant amount the rate of thermal diffusion from the defect.

Another model views the defect site as important in the generation of hole-electron pairs.

The absorptivity, α , is a function of the crystalline perfection of the silicon. The value for amorphous silicon exceeds that for crystalline silicon by an order of magnitude.⁽¹⁰⁾ This suggests that the absorption of laser energy at a defect site is much higher than in adjacent undamaged silicon. According to this view, we would generate high concentrations of holes and electrons around individual defect sites. We recognize that the recombination rate is proportional to the hole-electron concentration product, i.e., $R = r [n][p]$. An increase in the electron and hole concentrations of an order of magnitude results in an increase in the recombination rate of two orders of magnitude. The rate of diffusion of excess holes and electrons away from the defect site where they were generated will be proportional to their concentration

gradient and hence to their concentration. This is significantly less than the rate of recombination, insuring that recombination and hence thermal release occurs at the defect sites where the hole-electron pairs were generated.

On the basis of available evidence we are unable to decide whether either or both of these suggested models are valid.

In our results we found that repeated lower energy pulses, i.e., .5 and 1.0 J cm⁻² resulted in no greater solution of defect nuclei than occurs with a single pulse. It would appear that the first pulse dissolves some of the primary defect nuclei while converting others due to released thermal energy into secondary defects. As shown in our second set of experiments, secondary defects are much more resistant to dissolution by laser pulsing, so that repeated pulsing contributes little to defect removal.

V. CONCLUSIONS

1. Pulsed laser annealing of lower fluence ion implants does not result in full electrical activation.
2. Laser anneal single pulse energies of 1.5 J cm⁻² are sufficient to dissolve implant defect nuclei in lower fluence ion implants without causing melting.
3. Following a pulsed laser anneal with thermal annealing permits us to obtain both dissolution

of implant defect nuclei as well as complete electrical activation without redistribution of low fluence ion implanted impurities.

4. A two step thermal anneal followed by a pulsed laser anneal permits us to obtain both dissolution of implant defect nuclei, as well as complete electrical activation without impurity redistribution, for implant fluences sufficiently high to cause amorphism at the surface.

This work was supported in part by the Defense Advanced Research Projects Agency.

TABLE I
EXPERIMENTAL CONDITIONS

WAFER NUMBERS	TYPE	ORIENTATION	IMPLANT SPECIES	IMPLANT FLUENCE
113A, 113B	n	(100)	^{11}B	$1 \times 10^{14} \text{ cm}^{-2}$
114A, 114B	p	"	^{31}P	$1 \times 10^{14} \text{ cm}^{-2}$
115A, 115B	n	"	^{11}B	$5 \times 10^{14} \text{ cm}^{-2}$
116A, 116B	p	"	^{31}P	$5 \times 10^{14} \text{ cm}^{-2}$
117A, 117B	n	"	^{11}B	$1 \times 10^{15} \text{ cm}^{-2}$
213A, 213B	n	(111)	^{11}B	$1 \times 10^{14} \text{ cm}^{-2}$
214A, 214B	p	"	^{31}P	$1 \times 10^{14} \text{ cm}^{-2}$
215A, 215B	n	"	^{11}B	$5 \times 10^{14} \text{ cm}^{-2}$
216A, 216B	p	"	^{31}P	$5 \times 10^{14} \text{ cm}^{-2}$
217A, 217B	n	"	^{11}B	$1 \times 10^{15} \text{ cm}^{-2}$

Boron implantations at 50 keV

Phosphorus implantations at 80 keV

TABLE II

SHEET RESISTANCES OF BORON IMPLANTED
WAFERS FOLLOWING LASER ANNEAL

WAFER NUMBER	IMPLANT FLUENCE B CM ⁻²	SHEET RESISTANCE Ω/\square			
		LASER ENERGY, JOULES PER CM ²			
		1.0	1.5	2.0	2.5
113A	1x10 ¹⁴	---	1712	877	886
213A		---	975	907	794
115A	5x10 ¹⁴	1374	407	256	270
215A		747	306	239	246
117A	1x10 ¹⁵	5312	280	127	128
217A		3372	406	124	124

TABLE III

SHEET RESISTANCES OF PHOSPHORUS IMPLANTED
WAFERS FOLLOWING LASER ANNEAL

WAFER NUMBER	IMPLANT FLUENCE P CM ⁻²	SHEET RESISTANCE, Ω/\square			
		LASER ENERGY, JOULES PER CM ²			
		1.0	1.5	2.0	2.5
114A	1x10 ¹⁴	---	682	480	459
214A		---	766	493	450
116A	5x10 ¹⁴	386	200	162	155
216A		435	185	148	145

TABLE IV

SHEET RESISTANCE IN Ω/\square OF LASER ANNEALED AREAS
FOLLOWING THERMAL ANNEAL OF 10 MINUTES
AT 1000°C IN N₂ AMBIENT

SPECIMEN	LASER BEAM ENERGY, JOULES PER CM ²				
	0	1.0	1.5	2.0	2.5
113	619	710	714	660	658
114	409	395	400	397	390
115	193	189	191	188	190
116	139	132	131	130	130
117	113	106	102	103	99
213	655	675	690	661	650
214	393	416	409	402	395
215	199	199	194	194	192
216	150	148	144	137	136
217	109	107	109*	104	102

* Reduced area due to fracture of wafer

TABLE V

EFFECT OF LASER ANNEAL ENERGIES ON THE GENERATION OF
OXIDATION EXPANDED DEFECTS

SPECIMEN NUMBER	LASER PULSE ENERGIES, J CM ⁻²					NON-IMPLANTED NONE
	NONE	1.0	1.5	2.0	2.5	
113B1	light OSF	heavy OSF	light OSF (spotty)	small SF	small SF	clear
213B1	light OSF	light OSF	no OSF	no OSF	no OSF	no OSF
114B1	heavy DL	heavy DL (spotty)	random circular pits	random circular pits	random circular pits	discrete elongated pits
214B1	heavy OSF	heavy OSF (spotty)	no OSF	no OSF	no OSF	no OSF
115B1	heavy OSF	heavy OSF	no OSF	no OSF	no OSF	no OSF
	- - background	- - reduced background	- - clear background	- - clear background	- - clear background	- - clear background
215B1	heavy OSF	heavy OSF (50% area clear)	few discrete OSF	no OSF	no OSF	no OSF
116B1	heavy OSF	heavy OSF	no OSF	no OSF	no OSF	no OSF
	- - background	- - reduced background	- - clear background	- - clear background	- - clear background	- - clear background
216B1	heavy background	reduced background	reduced background	clear background	clear background	clear background
117B1	heavy OSF	heavy OSF	no OSF	no OSF	no OSF	no OSF
	- - background	- - clear background	- - clear background	- - clear background	- - clear background	- - clear background
217B1	heavy OSF	heavy OSF (15% area clear)	few discrete OSF	no OSF	no OSF	no OSF

TABLE VI
EFFECT OF LASER ANNEAL ENERGIES ON THE GENERATION
OF OXIDATION EXPANDED DEFECTS IN THERMALLY ANNEALED SPECIMENS

SPECIMEN NUMBER	LASER PULSE ENERGIES, J cm ⁻²					NON-IMPLANTED NONE
	NONE	1.0	1.5	2.0	2.5	
113B2	light OSF	light OSF	light OSF	light OSF	light OSF	light OSF
213B2	heavy circular pits	heavy circular pits	heavy circular pits	heavy circular pits	heavy circular pits	heavy circular pits
114B2	heavy DL	heavy DL	heavy DL (light DL in areas)	light DL	light DL	clear
214B2	light OSF	light OSF	light OSF	light OSF	light OSF	light OSF
115B2	heavy OSF background	heavy OSF background	heavy OSF reduced background (in areas)	heavy OSF reduced background	reduced OSF clear background	no OSF clear background
215B2	heavy OSF background	heavy OSF background	reduced OSF (in areas) background	reduced OSF reduced background	reduced OSF clear background	no OSF clear background
116B2	heavy OSF background	heavy OSF background	reduced OSF 5% clear background	reduced OSF 30% clear background	reduced OSF clear background	no OSF clear background
216B2	heavy OSF background	heavy OSF background	reduced OSF reduced background	no OSF clear background	no OSF clear background	no OSF clear background
117B2	heavy OSF background	heavy OSF background	heavy OSF background	reduced OSF (in areas) background	reduced OSF clear background	no OSF clear background
217B2	heavy OSF background	heavy OSF background	reduced OSF reduced background	reduced OSF clear background	no OSF (50% of area) clear background	no OSF clear background

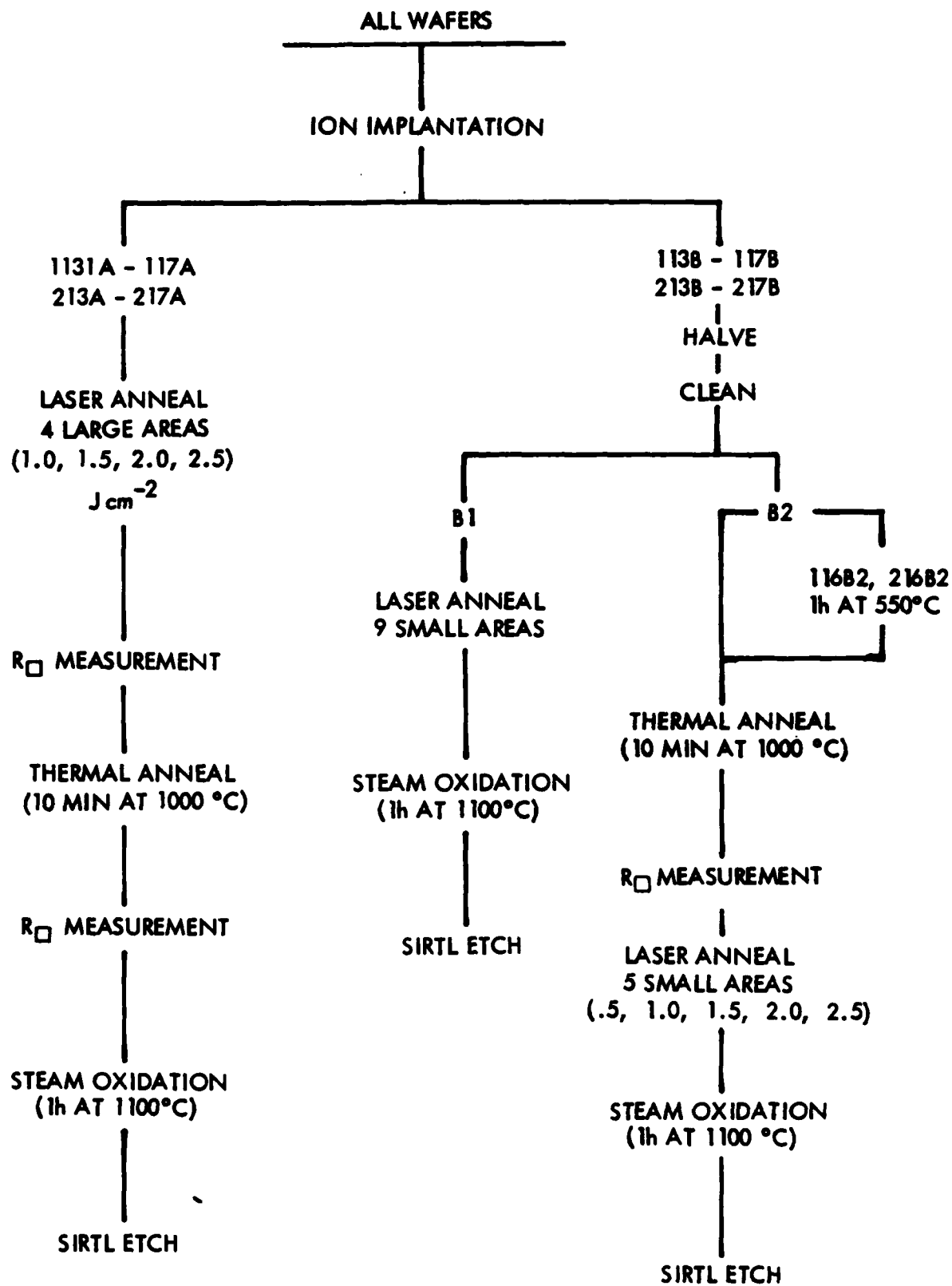


Figure 1. Flow Diagram of Experiments

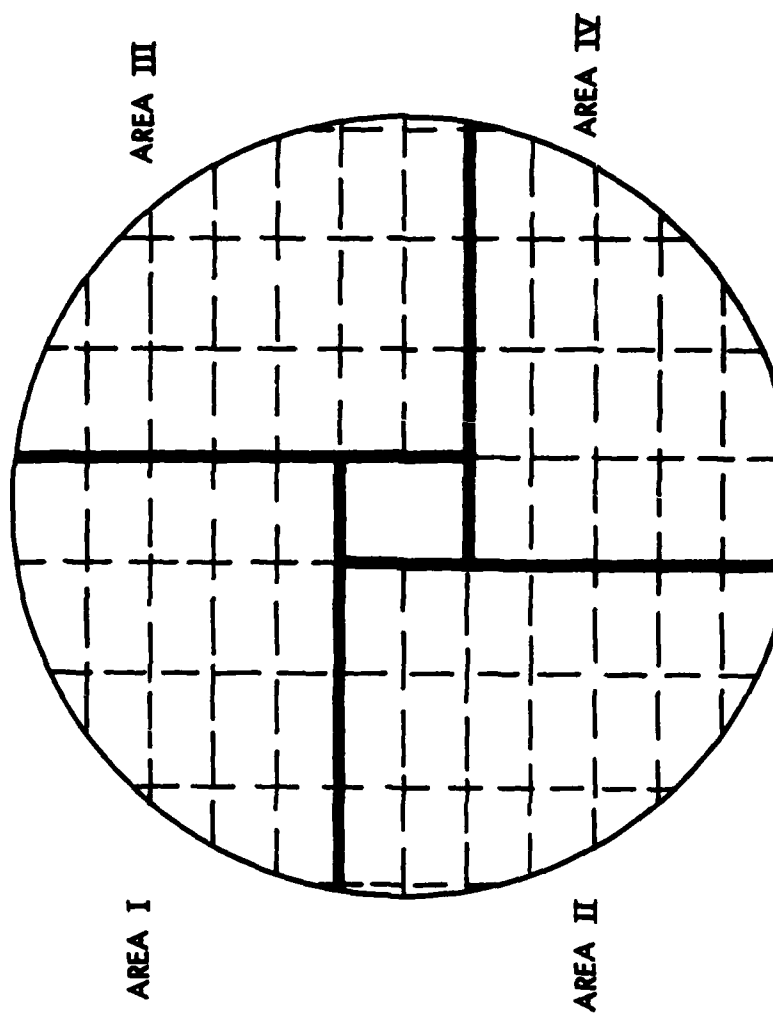


Figure 2. Distribution of Laser Pulses. Area I (1.0 J cm^{-2}),
Area II (1.5 J cm^{-2}), Area III (2.0 J cm^{-2}),
Area IV (2.5 J cm^{-2}).

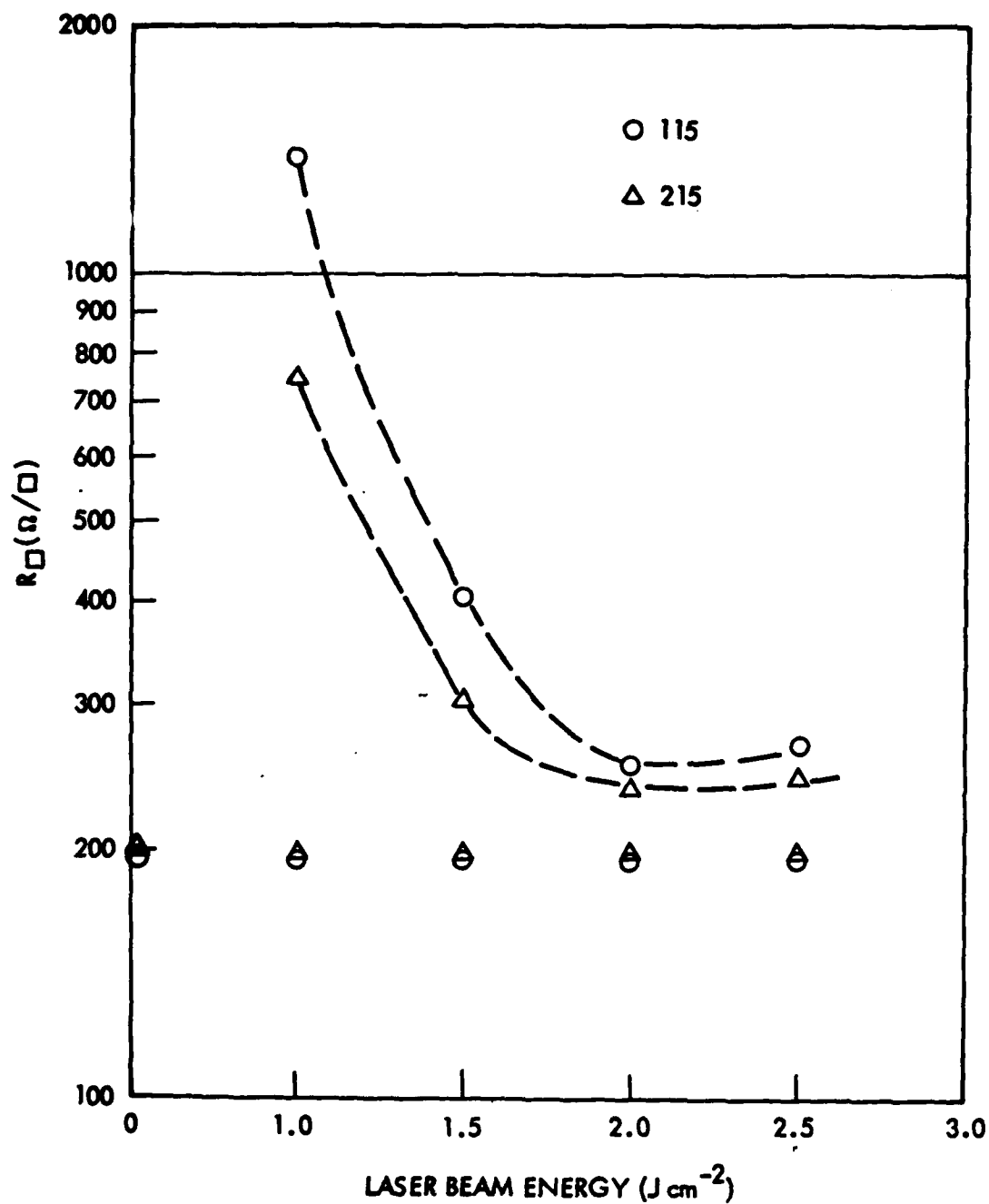


Figure 3. Comparison of Laser Annealing and Laser Plus Thermal Annealing of Sheet Resistances of $5 \times 10^{14} \text{ Bcm}^{-2}$ Implanted Wafers

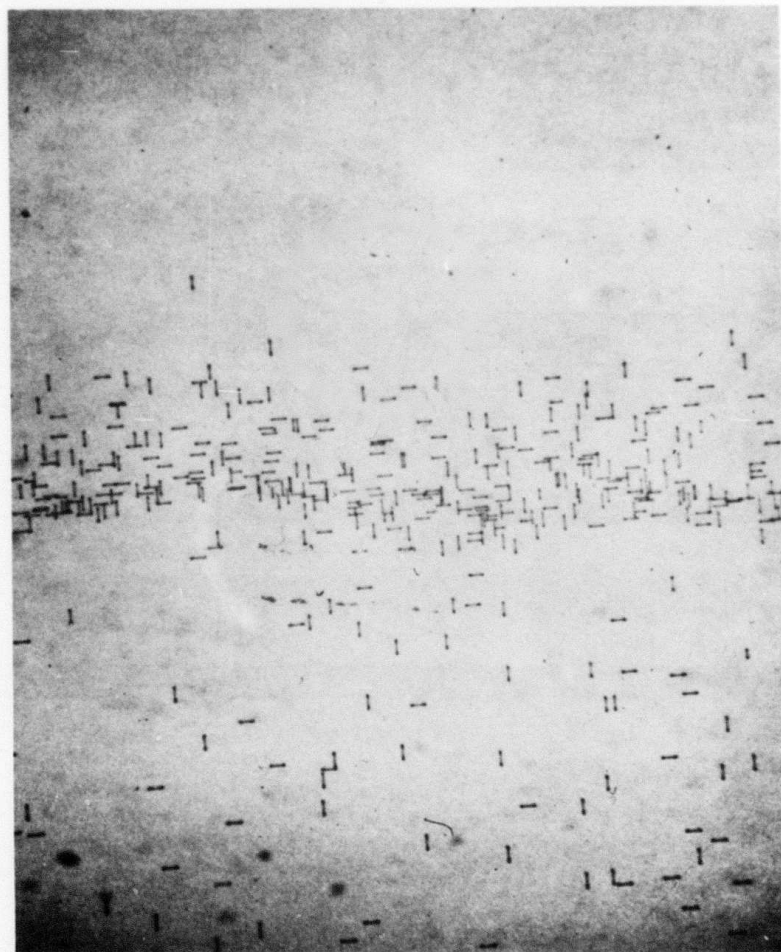


Figure 4. Laser Pulse Boundary for Specimen 113B1.
 1×10^{14} B cm⁻², 1.5 J cm⁻² Laser Energy,
Sirtl Etch 10 Secs, Mag. 100X.

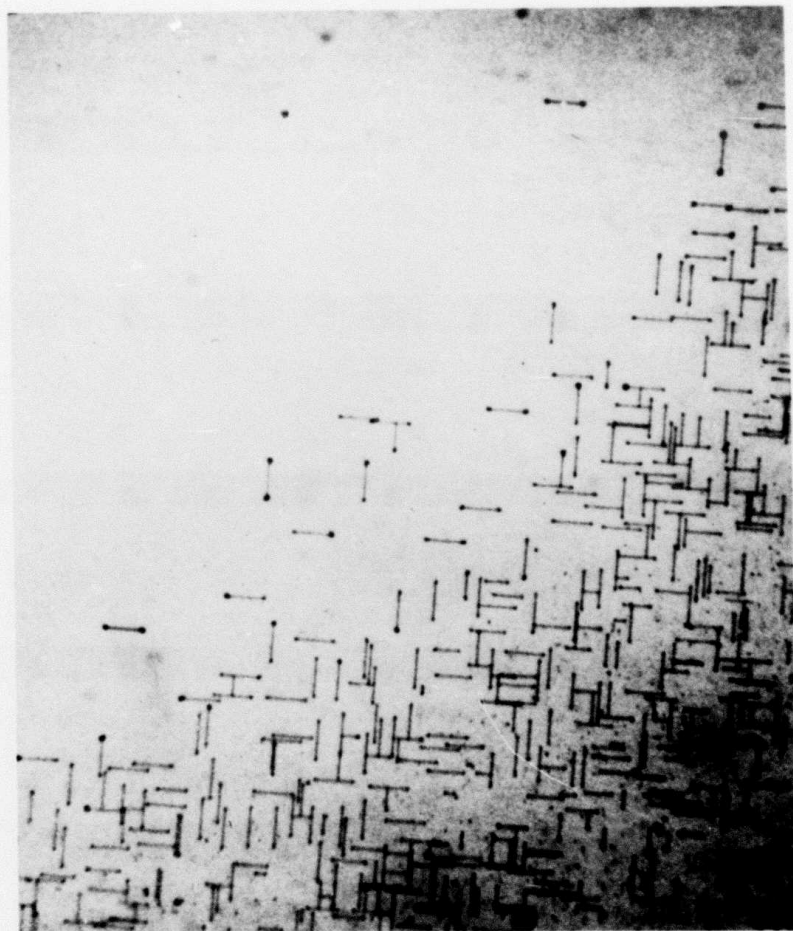


Figure 5. Laser Pulse Boundary for Specimen 117B1.
Junction of Laser Annealed and Transition
Area. $1 \times 10^{15} \text{ B cm}^{-2}$, 1.5 J cm^{-2} Laser
Energy, Sirtl Etch 10 Secs, Mag. 250X.

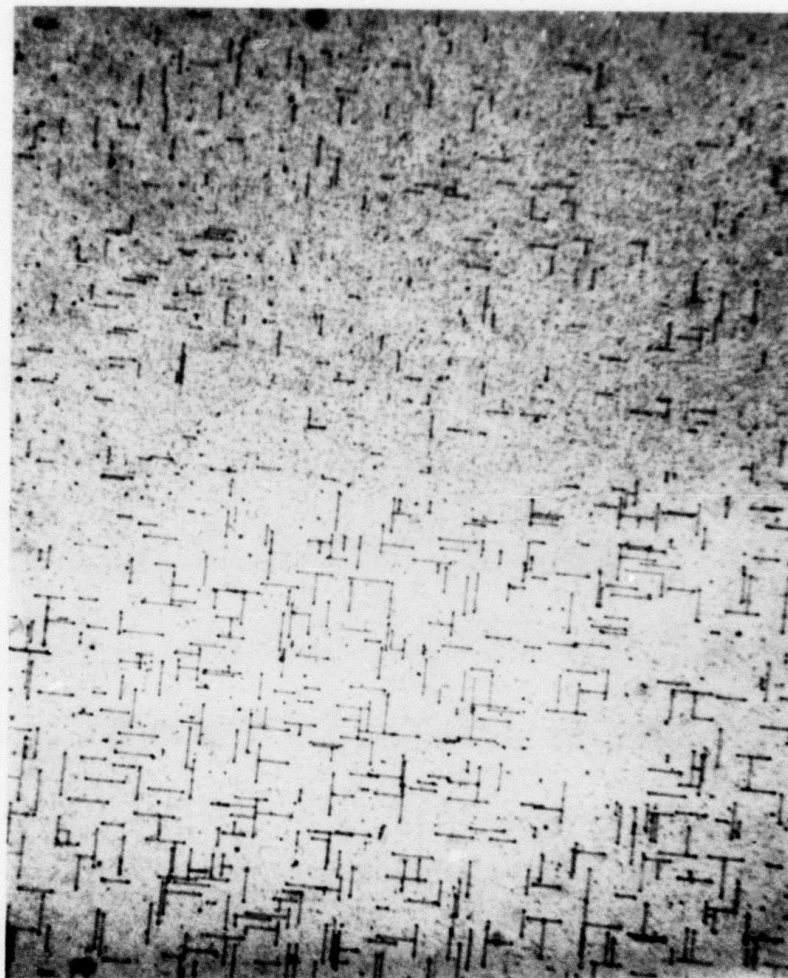


Figure 6. Laser Pulse Boundary for Specimen 117B1.
Junction, Unannealed, and Transition Area.
 $1 \times 10^{15} \text{ cm}^{-2}$, 1.5 J cm^{-2} Laser Energy,
Sirtl Etch 10 Secs, Mag. 250X.



Figure 7. Scanning Electron Micrograph of Neutron
Irradiated Silicon Surface Exposed to a
Ruby Laser Pulse of 2.0 J cm^{-2} , Mag. 300X.

REFERENCES

1. Masao Tamur , Appl. Phys. Lett. 23, 651 (1973)
2. D.J. Mazey, R.S. Nelson and R.S. Barnes,
Phil. Mag., 17, 1145 (1968)
3. E. Bøgh, P. Høgild, and I. Stensgaard, Proc. 1st.
Int. Conf. Ion Implantation, L. Chadderton and
F. Eisen Eds. Gordon and Breach, New York(1971)
4. S. Prussin, J.Appl. Phys. 45, 1635 (1974)
5. C.W. White, J. Narayan, and R.T. Young
Science 204, 461 (1979)
6. A. Gat, J.F. Gibbons, T.J. Magee, J. Peng, V.R. Deline,
P. Williams, and C.A. Evans, Jr. Appl. Phys. Lett. 32,
276 (1978)
7. H.J. Leamy, G.A. Rozgonyi, T.T. Sheng and G.K. Celler,
Appl. Phys. Lett. 32, 535 (1978)
8. M. Miyao, N. Yoshihiro and T. Tokuyama,
J. Appl. Phys. 50, 223 (1979)
9. L. Csepregi, W.K. Chu, H. Muller, J.W. Mayer and
T.W. Sigmon, Radiat. Eff. 28, 227 (1976)
10. P. Baeri, S.U. Campisano, G. Foti, and E. Rimini,
Appl. Phys. Lett. 33, 137 (1978)